Patterns and trends of frontal activity in Australian marine hotspots

by

Kai Yang

(University of Tasmania)

A thesis submitted in partial fulfilment of the requirements of the Bachelor of Marine and Antarctic Science with Honours at the Institute for Marine and Antarctic Studies (IMAS), University of Tasmania (July, 2020).

Declaration

This thesis contains no material which has been accepted for the award of any other degree or diploma in any tertiary institution, and to the best of my knowledge and belief, contains no material previously published or written by another person, except where due reference is made in the text of the thesis.

Signed

Kai Yang

Kai Yang

Date： 10 July 2020

Abstract

Oceanic fronts, the junction between water masses, are ubiquitous in the global ocean. It has been suggested that biological productivity and the abundance of marine species are correlated with frontal activity. Ocean warming due to climate change may lead to long-term changes in frontal activity, due to, for example, changes in regional and local current systems. In this study, the variability and trends of thermal fronts in two marine hotspots near Australia were investigated using two frontal detection methods and two different satellite sea surface temperature datasets. Six- and eight-day average frontal maps were generated to make a visual comparison between the frontal detection methods and to compute several parameters of frontal activity spanning 26 years (1993-2018). These parameters included frontal density (FD) and monthly and annual composites of frontal probability (probability of frontal encounter, PFE). Visually, fronts detected by the two methods clearly separate SST populations in frontal maps. The Canny gradient-based method detected more fronts than the single image edge detection method, while the latter method performed better in processing data in areas of poor coverage. The interannual trends of FD and PFE all follow gently increasing trends in both Australian hotspots, but some of the increasing trends are not statistically significant. In addition, both FD and PFE showed significant seasonal cycles, being higher in austral summer months and lower in winter months, and frontal activity is more prevalent in coastal areas and lower latitudes. The frontal maps generated in this study, when integrated with other oceanographic data, can provide further insight into the structure and processes of thermal fronts. The overall trends and seasonal cycles can be important for understanding the impact of ocean warming on marine ecosystems and biodiversity.

Acknowledgement

Firstly, I would like to express my deep gratitude to Dr Andrew Fischer, my research supervisor, for his patient guidance, enthusiastic encouragement and useful critiques of this Honours research. I would also like to thank one of his Honours student, Mr Jia Sheng Danny Tan, for his help in applying the Mann-Kendall test. My grateful thanks are also extended to Dr Helen Philips, Dr Stuart Corney, Professor Neil Holbrook for their assistance and useful feedback in the final seminar, to Dr Hakase Hayashida for proof-reading.

I would also like to extend my thanks to my classmates and friends of the University of Tasmania and Ocean University of China for their accompany at such a difficult time.

Finally, I wish to thank my parents and my girlfriend for their support and encouragement throughout my study.

Table of contents

Declaration 2

Abstract 3

Acknowledgement 4

Table of contents 5

List of figures and tables 7

Chapter 1 Introduction 11

1.1. Oceanic fronts 11

1.1.1. Definition of fronts 11

1.1.2. Ecological roles of fronts 11

1.1.3. Factors leading to the formation of fronts 12

1.2. Fronts and climate change 13

1.3. Detecting oceanic fronts 14

1.4. Study aims 15

Chapter 2 Data and methods 17

2.1. Study regions 17

2.2. Satellite Data 18

2.3. Edge Detection Algorithms 20

2.3.1. Adaptive Canny (1986) Gradient-based Algorithm 21

2.3.2. Cayula and Cornillon (1992) SIED Method 23

2.4. Frontal Analysis 25

Chapter 3 Results 27

3.1. Analysis of SST data 27

3.2. Analysis of the two frontal detection methods (Aim 1) 28

3.2.1. Adaptive Canny algorithm 28

3.2.2. Cayula and Cornillon SIED algorithm 29

3.2.3. **Algorithm Comparison** 30

3.3. Trend Analysis (Aim 2) 37

3.3.1. **AVHRR results** 37

3.3.2. **MODIS results** 45

3.4. Modified Mann-Kendall test (Aim 2) 52

Chapter 4 Discussion 54

4.1. Comparison between the edge detection algorithms and the SST products (Aim 1) 54

4.2. Trends of frontal activity (Aim 2) 57

4.3. Future research 61

References 62

List of figures and tables

Figures

Figure 2.1 Overlap of the distribution of the major marine hotspot regions based on two historical SST datasets (Had1SST and ERSST) (Hobday & Pecl 2014, Figure 1c). 17

Figure 2.2 The South West and South East Australia hotspot study regions. The South West Australia (SW) study region is located between 21°55' S, 88°52' E to 43°22' S, 117°29' E and the South East Australia (SE) study region is located between 25° S, 146° E to 43° S, 161° E. The images of the two the study regions show SST on 26 December 2015, derived from the Advanced Very High-Resolution Radiometer (AVHRR). Black lines in the image represent fronts detected by the Canny edge detection algorithm. 18

Figure 3.1 Annual average data quality of SST datasets used in this study for the South East (SE) and South West (SW) study regions for Advanced Very-High-Resolution Radiometer (AVHRR) and Moderate Resolution Imaging Spectroradiometer (MODIS) datasets. 28

Figure 3.2 Examples of high and low data-quality SST images within the Advanced Very-High-Resolution Radiometer (AVHRR) dataset. 28

Figure 3.3 Frontal maps derived from the AVHRR SST data using the Adaptive Canny gradient-based algorithm in (a) the SE study region and (b) the SW study region. The images contain SST data from 26 December 2015 using the Advanced Very High-Resolution Radiometer (AVHRR). Black lines are thermal fronts and white areas indicate missing SST data. 32

Figure 3.4 Frontal maps derived from the MODIS SST data using the Adaptive Canny gradient-based algorithm in (a) the SE study region and (b) the SW study region. The images show SST data from 26 December 2015 using the Moderate Resolution Imaging Spectroradiometer (MODIS). Black lines are thermal fronts and white areas indicate missing SST data. 33

Figure 3.5 Frontal maps derived from the AVHRR SST data using the Cayula and

Cornillon SIED algorithm in (a) the SE study region and (b) the SW study region. The images show SST data from 26 December 2015 using the Advanced Very High-Resolution Radiometer (AVHRR). Black lines are thermal fronts and grey areas indicate missing data...34

Figure 3.6 Frontal maps derived from the MODIS SST data using the Cayula and Cornillon SIED algorithm in (a) the SE study region and (b) the SW study region. The images show SST data from 26 December 2015 using the Moderate Resolution Imaging Spectroradiometer (MODIS). Black lines are thermal fronts and grey areas indicate missing data...35

Figure 3.7 Time series of annual probability of frontal encounter (PFE) in the South East Australia (SE) study region based on different edge detection algorithms...36

Figure 3.8 Annual probability of frontal encounter (PFE) images of the South East Australia (SE) study region derived from the Advanced Very High-Resolution Radiometer (AVHRR) data. Thermal front detection is based on the Adaptive Canny Gradient-based Algorithm. P1 is the period of 1993 to 2000, P2 is the period of 2001 to 2005 and P3 is between 2006 to 2018. White areas indicate a PFE of 0. 38

Figure 3.9 Time series of (a) the 6-day average FD, (b) the monthly average PFE and (c) the annual average PFE for the SE study region using the Advanced Very High-Resolution Radiometer (AVHRR) SST data. Thermal fronts were detected by the Adaptive Canny Gradient-based Algorithm. FD is frontal density. PFE is the probability of frontal encounter. P1 denotes the period between 1993 to 2000, P2 between 2001 to 2005 and P3 between 2006 to 2018. 39

Figure 3.10 Annual probability of frontal encounter (PFE) images of the South West Australia (SW) study region derived from the Advanced Very High-Resolution Radiometer (AVHRR) data. Thermal front detection is based on the Adaptive Canny Gradient-based Algorithm. P1 is the period of 1993 to 2000, P2 is the period of 2001 to 2005 and P3 is between 2006 to 2018. White areas indicate a PFE of 0. 43

Figure 3.11 Time series of (a) 6-day average FD, (b) monthly average PFE and (c) annual average PFE for the SW study region using the Advanced Very High-Resolution Radiometer (AVHRR) SST data. Thermal front detection was based on the Adaptive Canny Gradient-based Algorithm. FD is frontal density. PFE is the probability of frontal encounter. P1 denotes the period between 1993 to 2000, P2 between 2001 to 2005 and P3 between 2006 to 2018; 44

Figure 3.12 Annual probability of frontal encounter (PFE) images of the South East Australia (SE) study region derived from the Moderate Resolution Imaging Spectroradiometer (MODIS) data. Thermal front detection is based on the Adaptive Canny Gradient-based Algorithm. P1 is the period of 1993 to 2000, P2 is the period of 2001 to 2005 and P3 is between 2006 to 2018. White areas indicate a PFE of 0. 47

Figure 3.13 Time series of (a) the 6-day average FD, (b) the monthly average PFE and (c) the annual average PFE for the SE study region using the Moderate Resolution Imaging Spectroradiometer (MODIS) SST data. Thermal front detection was based on the Adaptive Canny Gradient-based Algorithm. FD is frontal density. PFE is the probability of frontal encounter 48

Figure 3.14 Annual probability of frontal encounter (PFE) images of the South West Australia (SW) study region derived from the Moderate Resolution Imaging Spectroradiometer (MODIS) data. Thermal front detection is based on the Adaptive Canny Gradient-based Algorithm. P1 is the period of 1993 to 2000, P2 is the period of 2001 to 2005 and P3 is between 2006 to 2018. White areas indicate a PFE of 0. 50

Figure 3.15 Time series of (a) the 6-day average FD, (b) the monthly average PFE and (c) the annual average PFE for the SW study region using the Moderate Resolution Imaging Spectroradiometer (MODIS) SST data. Thermal front detection was based on the Adaptive Canny Gradient-based Algorithm. FD is frontal density. PFE is the probability of frontal encounter. 51

Tables

Table 2.1 Spatial and temporal resolution, data product type and source of the Moderate Resolution Imaging Spectrometer (MODIS) and the Advanced Very High-Resolution Radiometer (AVHRR) SST products used in this study. 20

Table 3.1 Comparison of the mean values of the smoothed FD (red curve in Figure 3.9a), smoothed monthly PFE (red curve in Figure 3.9b) and annual PFE (Figure 3.9c) in P1 and P3 (results from AVHRR SST data of the South East Australia (SE) study region). P1 is between 1993 to 2000 and P3 is the period between 2006 to 2018. 40

Table 3.2 Comparison of the mean values of the smoothed FD (red curve in Figure 3.11a), smoothed monthly PFE (red curve in Figure 3.11b) and annual PFE (Figure 3.11c) in P1 and P3 (results from AVHRR SST data of the South West Australia (SW) study region). P1, Period of 1993 to 2000; P3, Period of 2006 to 2018; 45

Table 3.3 Results of the Modified Mann–Kendall test applied to serially correlated data. The test was applied to results from the Advanced Very-High-Resolution Radiometer (AVHRR)/Moderate Resolution Imaging Spectroradiometer (MODIS) data over the South East Australia study region (SE) and the South West Australia study region (SW), using the Cayula and Cornillon SIED algorithm (SIED)/Adaptive Canny gradient-based algorithm (Canny). APFE, the annual probability of frontal encounter; MPFE, the monthly probability of frontal encounter; FD, frontal density; 53

Chapter 1 Introduction

1.1. Oceanic fronts

1.1.1. Definition of fronts

Oceanic fronts are defined as sharp gradients at the junction of two adjacent water masses, which usually have different physical, biochemical and optical properties (Belkin 2009). Fronts are typically regions of intensified mixing, increased turbulence and convection (Roden 1976). In the global ocean, fronts occur across different spatial and temporal scales. This is due to many factors such as topography (Wolanski & Hamner 1988) and various atmospheric and oceanic conditions (Wai & Stage 1989; Belkin et al. 2007). As a result, there are many types of frontal features as identified in Belkin (2002), including mid-shelf fronts, shelf-slope fronts, equatorial upwelling fronts and boundary current fronts. The length scale of fronts can be several kilometres (fronts near rivers and estuaries) to thousands of kilometres (ocean current fronts) (Joseph 2014). Across time scales, fronts can last for a few minutes or be seasonal features (Joseph 2017). The boundaries of fronts sometimes can be easily observed visually from a ship without any instruments.

1.1.2. Ecological roles of fronts

Mixing of water masses may occur near fronts regardless of whether the water masses are converging or diverging. Water movement and mixing can increase physical and biological activity near fronts through the transfer of nutrients or by creating suitable physical conditions (Sato et al. 2018). This activity can further influence local marine ecosystems (Brandini et al. 2018). The presence of fronts can change the composition of the plankton community and associated biogeochemical fluxes (Landry et al. 2012; Stukel et al. 2017). Fronts can also drive productivity flows in ecosystems and affect the distribution of species (Woodson & Litvin 2015) such as bluefin tuna (Fiedler & Bernard 1987; Royer et al. 2004; Xu et al. 2017). By driving nutrients through alternate trophic pathways, fronts can also increase total ecosystem biomass and enhance fisheries production (Woodson & Litvin 2015). Oceanic fronts are abundant in upwelling systems (Mauzole et al. 2020) and play an important role in predator-prey interactions and energy transfer through food webs (Sato et al. 2018) and increase the abundance of forage fish and top predators (Snyder et al. 2017). In the Southern Ocean, fronts strongly influence exchanges among the ocean, atmosphere and cryosphere, and are of fundamental importance to the climate system (Williams et al. 2007; Sallée et al. 2008; Chapman et al. 2020).

1.1.3. Factors leading to the formation of fronts

Several factors are responsible for the formation of fronts. Firstly, topography (Wolanski & Hammer 1988) can lead to the development of fronts in both the open ocean and near coasts. In the open ocean, topographic features such as seamounts can lead to the formation of vertical fronts and eddies. The influence of topography is stronger near coasts due to complex bathymetric features (Levine & White 1983; Wolanski & Hamner 1988; Wall et al. 2008) and the hydrodynamic influence of estuarine and riverine flux (Fischer et al. 2017). Consequently, coastal fronts are more complex and variable than open-ocean fronts, especially when interacting with tides. Another example is the influence of the continental shelf (Holladay & O'Brien 1975) and the shelf break (Condie 1993).

Prevailing atmospheric and oceanic conditions are also important factors in the formation of fronts. Spatial variation of wind stress at the sea surface drives the horizontal movement of surface water, leading to either convergence or divergence of different water masses (Heath 1972). Upwelling and downwelling can lead to the movement of water from depth to the surface and from the surface to depth, respectively. As a result, fronts can have a vertical expression at depth depending on the strength of the phenomena (Brink 1987; Letelier et al. 2009). Furthermore, bathymetric, atmospheric and oceanic features can drive the spatial variability of the entire frontal structure (Chapman et al. 2020). Chapman et al. (2020) noted that regionally localised southward shifts of the

Antarctic Circumpolar Current fronts are driven by changes in winds, leading to changes in local frontal activity and warming in the Southern Ocean.

1.2. Fronts and climate change

It has been suggested that climate change has influenced the formation of fronts in the last few years, leading to changes in their probability, density and distribution of frontal activity. Consequently, such changes will affect the function and diversity of the local ecosystems that are dependent on frontal activity.

Several studies noted that there are relationships between changes in atmospheric forcing due to large-scale climate modes such as El Niño/La Niña and changes in local frontal activity (Sallée et al. 2008; Kim & Orsi 2014; Chapman et al. 2020). Many studies have focused on long-term trends of frontal activity. However, there is lack of consensus in the literature regarding these trends under scenarios warming seas and climate change. Several trends have been suggested in recent years. Kahru et al. (2012) looked at frontal trends in the California Current System (CCS) and suggested a long-term increasing trend in frontal frequency in the CCS region. The findings of Kahru et al. (2012) are derived from the study of 29-year (1981-2009) sea surface temperature and 14-year (1997-2010) chlorophyll datasets. Conversely, Kahru et al. (2018) focused on the influence of warm anomalies between 2014 and 2016 in the North-East Pacific. It was suggested that the frequency of fronts decreased significantly as a result of warm anomalies (Kahru et al. 2018). Whether this decline represents the beginning of a new long-term decreasing trend or is just an interruption in the long-term increasing trend previously suggested by Kahru et al. (2012) remains an open question (Kahru et al. 2018). Oerder et al. (2018) also found an increasing trend of frontal frequency near the coast of Central Chile. Furthermore, Obenour (2013) had suggested that the long-term trends of frontal activity as a result of climate change was not uniform in the global ocean. Overall, the global probability of fronts has increased linearly at a rate of 0.25% per decade over 30 years (Obenour 2013).

Ocean warming due to climate change is not distributed evenly across the global ocean. Marine heatwaves (MHWs) have also become longer and more frequent over the past decades (Oliver et al. 2018) affecting selected regions of the global ocean. Intense regional warming can be manifested in marine hotspots, or areas that are warming faster than 90% of the global ocean (Hobday & Pecl 2014). In these hotspots, the impacts of ocean warming on ecosystems will likely be observed earlier. For example, Bakun (1990) proposed that global warming would lead to an intensification of coastal upwelling circulation by amplifying alongshore winds due to increased onshore-offshore atmospheric-pressure gradients. This intensification will then lead to an enhancement in frontal probability (Obenour 2013), which will likely occur earlier in marine hotspots than other areas. Additional frontal studies over these regions are important to resolve the previous discrepancies in findings and can provide knowledge to enable resource managers to adapt to the impacts of global ocean warming and intensive MHWs.

1.3. Detecting oceanic fronts

Remotely sensed imagery is widely used to find oceanic fronts. Most studies use sea surface temperature (SST) and chlorophyll-a concentrations (Chl) derived from satellite radiance values. Several methods have been proposed to extract frontal information from satellite imagery, including a variety of edge detection algorithms. These algorithms range from simple edge operators for characterising horizontal gradient of a field (Canny 1986; Sobel & Feldman 1973; Prewitt 1970) to more sophisticated algorithms such as cluster-shade analysis (Holyer & Peckinpaugh 1989), histogram analysis (Cayula & Cornillon 1992; Saraceno et al. 2005), entropy analysis based on the Jensen-Shannon divergence (Vázquez et al. 1999), and semivariogram analysis (Diehl et al. 2002).

The two commonly-used methods for detecting thermal or Chl fronts are the gradient-based method and histogram analysis. Among the edge detection algorithms developed so far, the Canny gradient-based method is one of the strictest edge defining methods (Canny 1986). The strictness in edge detection and simplicity of process for implementation make this method a popular choice for detecting marine fronts (Etnoyer et al. 2006; Wall et al. 2008; Miltiadou et al. 2018). The histogram analysis developed by Cayula and Cornillon (1992) is originally designed for detecting thermal fronts in SST images. Considering its ability of handling of cloud contamination in the original SST data (Cayula & Cornillon 1992), this method has an irreplaceable position in detecting thermal fronts (Hickox et al. 2000; Wall et al. 2008). Both of these methods were used and compared in this study.

1.4. Study aims

Given the varying findings with regards to trends in frontal activity in the global ocean under changing climate conditions, there is an increasing need to verify frontal trends, particularly in areas where ocean warming, due to anthropogenic climate change, has had a profound impact. To this end, the aim of this research is to detect marine fronts in SST images of marine hotspot regions near Australia using two independent edge detection algorithms (the adaptive Canny (1986) gradient-based algorithm and the Cayula and Cornillon (1992) single image edge detecting (SIED) algorithm) and two SST datasets to further analyse and verify trends in frontal activity.

This study set out to:

1) test and compare the performance of two frontal detection algorithms on two SST datasets of two different spatial resolutions;
2) determine whether fronts in two hotspot regions have changed in the probability over the course of a recent period of ocean warming due to climate change.

We hypothesise that the differences in the spatial resolution of datasets and detection principles lead to varied performance of the two algorithms. It is anticipated that despite the varying magnitude of frontal probability across the two algorithms and datasets, the general patterns and trends of frontal activity will be similar. According to the growth rate of 0.25% per decade of global frontal probability given by Obenour (2013), we hypothesise that the frontal probability and density both follow a gently increasing monotonous trend, however, interannual variations may result from climactic events, such as El Niño/La Niña. Regional differences may manifest themselves through the expression of changes to the strength and patterns of regional current systems.

Chapter 2 Data and methods

2.1. Study regions

This research mainly focuses on frontal activity in global marine hotspot regions, identified by Hobday and Pecl (2014). Hobday and Pecl (2014) calculated the linear trend in SST for each 1° × 1° pixel over 50 years (1950-1999) and used pixels with a high absolute temperature increase (highest 10%) to identify warming areas. Those warming areas larger than 25 square degrees were defined as hotspot regions (Hobday & Pecl 2014).

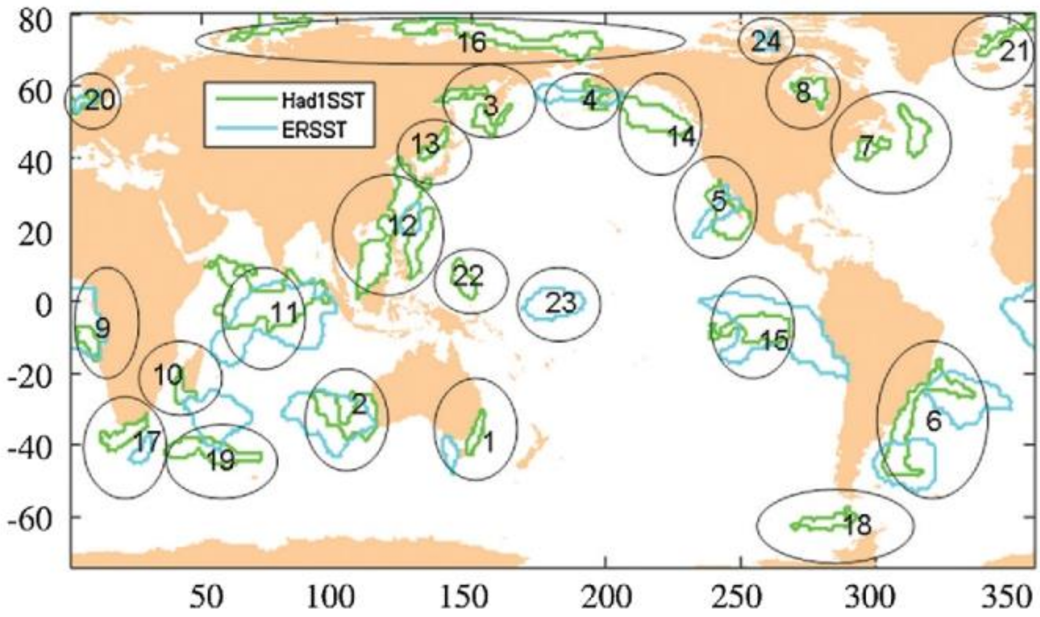

Figure 2.1 Overlap of the distribution of the major marine hotspot regions based on two historical SST datasets (Had1SST and ERSST) (Hobday & Pecl 2014, Figure 1c).

Specifically, this study examines two hotspot regions around Australia, Southeast Australia (SE) (Region 1) and Southwest Australia (SW) (Region 2) in Figure 2.1 (Hobday & Pecl 2014, Figure 1c). The study regions are represented as two rectangular areas (see Figure 2.2) that encompass the entire hotspot identified in Hobday and Pecl (2014). The SE study region was defined by a rectangular area with the upper-left corner at 25° S, 146° E and the lower-right corner at 43° S, 161° E (see Figure 2.2). This region extends about 950 km into the Tasman Sea from the East Coast of Australia, from Fraser Island to Hobart.

The SW study region was defined by a rectangular area with the upper-left corner at 21°55' S, 88°52' E and the lower-right corner at 43°22' S, 117°29' E (see Figure 2.2). This region extends about 2700 km southwest into the Indian Ocean from the west coast of Australia, from North West Cape to Albany. Both regions are affected by complex oceanographic conditions such as strong ocean currents, wind and freshwater inputs along the coasts, resulting in intense and complex frontal activity.

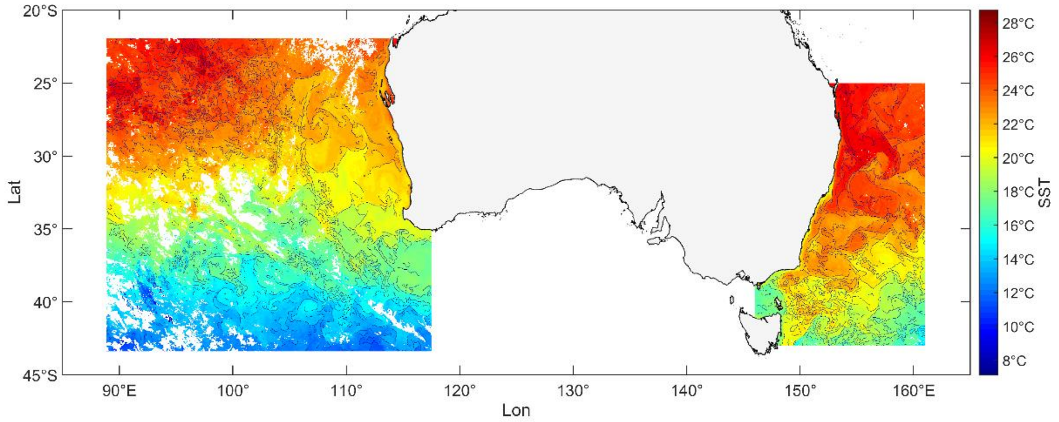

Figure 2.2 The South West and South East Australia hotspot study regions. The South West Australia (SW) study region is located between 21°55' S, 88°52' E to 43°22' S, 117°29' E and the South East Australia (SE) study region is located between 25° S, 146° E to 43° S, 161° E. The images of the two the study regions show SST on 26 December 2015, derived from the Advanced Very High-Resolution Radiometer (AVHRR). Black lines in the image represent fronts detected by the Canny edge detection algorithm.

2.2. Satellite Data

In this study, we used two satellite SST products to generate frontal maps. One SST product (Australia's Integrated Marine Observing System [IMOS] 2019) with a high spatial resolution (1.1 km × 1.1 km) was obtained by IMOS from the National Oceanic and Atmospheric Administration (NOAA) Advanced Very High-Resolution Radiometer (AVHRR) on all available NOAA Polar-orbiting Operational Environmental Satellites (POES). It is a satellite SST product detected only at the surface of the ocean (SST-skin product), available on the Australian Ocean Data Network (AODN). Each grid cell of this product contains the 6-day average of all the highest available quality SST data that overlaps with that cell, weighted by the area of overlap. Another SST product (Ocean Biology Processing Group [OBPG] 2015) with a 4×4 km spatial resolution was obtained from the NASA EOSDIS Physical Oceanography Distributed Active Archive Center (PO.DAAC) from NASA's Moderate Resolution Imaging Spectroradiometer (MODIS) on the Aqua satellite. It is an eight-day average SST-skin product (see Table 2.1). Both of the two products were day-time SST data (see Table 2.1).

For each study region, there are approximately 60 AVHRR SST images and 46 MODIS images for each year. In total, for each study region, we used 1538 AVHRR SST images over 1993-2018 and 736 MODIS SST images over 2003-2018 to detect fronts and analyse the trend in local frontal probability. SST datasets collected by two separate sensors cover different time periods and have different spatial resolutions. This not only helps to generate and analyse trends over different time periods, but also facilitates comparison and cross-validation across algorithms and datasets.

Two edge detection algorithms were applied to each of the two SST datasets. The adaptive Canny method was applied to all the AVHRR and MODIS SST images of the SE and SW study regions. The Cayula and Cornillon SIED method was mainly used to detect fronts for the SE study region from the AVHRR SST images (see Table 2.1).

Table 2.1 Spatial and temporal resolution, data product type and source of the Moderate Resolution Imaging Spectrometer (MODIS) and the Advanced Very High-Resolution Radiometer (AVHRR) SST products used in this study.

Sea Surface Temperature (SST) Data	Advanced Very High-Resolution Radiometer (AVHRR)	Moderate Resolution Imaging Spectrometer (MODIS)
Spatial resolution	1.1×1.1 km	4×4 km
Data product type	6-day-average/day-time	8-day-average/day-time
Data range	1993 - 2018	2003 - 2018
Source	https://portal.aodn.org.au/search	https://doi.org/10.5067/MODSA-8D4D4

2.3. Edge Detection Algorithms

The transition zone between two water masses with a large temperature difference can usually be observed with the naked eye in SST images. However, this process can be automated, and approaches such as edge detection algorithms allow for systematic extraction of oceanographic frontal features within the imagery.

The "Canny method," developed by Canny (1986), is a gradient-based algorithm. It defines edges by looking for local maxima of the gradient of a field, such as an SST field. The method detects horizontal gradients and produces the magnitude of the gradient as a continuous field which makes it simple to understand and use (Belkin & O'Reilly 2009). A test of the Canny method against a variety of other edge detection algorithms (Shrivakshan & Chandrasekar 2012) found that the Canny method performs better under noise. Therefore, this method was selected as one of the algorithms we used in this study. Due to its simplicity, we use this method to identify and examine fronts in all of the SST satellite images.

In addition to the Canny method, the population-based histogram algorithm developed by Cayula and Cornillon (1992) has been commonly applied to many marine surface signals such as SST and Chl to detect oceanographic fronts (SST: Cayula & Cornillon 1992, 1995; Ullman & Cornillon 1999, 2000, 2001; Belkin & Cornillon 2004; Chl: Stegmann & Ullman 2004; Bontempi & Yoder 2004). This method creates histograms from small independent windows of an image and examines whether there is a bimodal distribution to identify two water masses of different oceanographic characteristics, e.g., temperature. The original single image edge detection (SIED) histogram analysis was designed for detecting fronts in SST images. Several comparative studies (Cayula et al. 1991; Ullman & Cornillon 2000) between the performance of the Cayula and Cornillon (1992) SIED method and several other automated SST-detection methods found that SIED performed as well as or better than all of these methods. Due to the superior performance and wide application of the Cayula and Cornillon SIED method, it was selected and used in this study. However, because of the computationally intensive nature of the algorithm and the high-resolution SST data used, there was only enough time to process data using the SIED method or one of our study regions (the SE study region).

Parameters in both algorithms were modified to optimise their performance in processing the SST data. The description of these two algorithms and their specific modifications are provided below.

2.3.1. Adaptive Canny (1986) Gradient-based Algorithm

The edge detection of the Canny algorithm contains five steps. In the first step, the image is smoothed with a 2-D Gaussian filter. The basic principle of all edge detection algorithms is to define an edge by detecting the difference between two pixels. Noise in raw satellite-derived SST data can easily affect the detection. The purpose of smoothing is to minimise false detection due to the influence of obvious noise (e.g. s edges, processing errors, etc.). A 2-D isotropic Gaussian filter kernel of size $(2k+1) \times (2k+1)$ has the form:

$$G(i,j) = \frac{1}{2\pi\sigma^2} \exp\left(-\frac{(i-(k+1))^2 + (j-(k+1))^2}{2\sigma^2}\right) \quad (1)$$

where Sigma (σ) is the standard deviation of the Gaussian filter. In this study, a sigma of sqrt(2) was used, corresponding to a 7×7 kernel box ($k = 3$).

Second, the edge gradient of each pixel was computed. An edge in an SST image may point in many different directions. The Canny algorithm uses a 3×3 pixel window to decompose these directions. In a 3×3 pixel window, the direction of an edge can only go in four directions: horizontal, vertical and diagonal. In this way, the edge will be shown as its irregular shape when all the windows compose. The algorithm also computes the strength and direction of the edge gradient, which is assigned to the centre pixel of the window. The computation is given by

$$\text{Strength: } G = \sqrt{{G_x}^2 + {G_y}^2} \quad (2)$$

$$\Theta = \text{atan2}(G_y, G_x) \quad (3)$$

where G_x is the first derivative of the gradient in the horizontal direction and G_y is the first derivative of the gradient in the vertical direction

The third step is known as non-maximum suppression. Each edge extracted from the gradient value is usually wide because it usually contains two or more pixels in width. Non-maximum suppression helps to thin the edges by suppressing all the values of edge gradients to the local maxima. A multiple-pixel-width edge is suppressed to only one-pixel width. This is achieved by comparing the edge gradient strength of a pixel with the edge gradient strength of other pixels in both the positive and negative gradients direction.

Fourth, after applying non-maximum suppression, remaining edge pixels can represent real edges more accurately. However, there are still some edges that are caused by noise. Unlike the single threshold of other edge detection algorithms, the Canny method uses two thresholds: an upper gradient threshold and a lower gradient threshold. Edge pixels with gradient magnitude below the lower threshold are filtered out. Edge pixels with gradient magnitude above the higher threshold are marked as strong edge pixels. Those with gradient magnitude in between are marked as weak edge pixels. Then the Canny method checks the location of each weak edge pixel to see if it is directly adjacent to a strong edge pixel. If it is directly adjacent, the weak edge pixel is re-marked as a strong edge pixel. Pixel chains are formed by connecting strong edge pixels and these re-marked weak edge pixels.

Because the values of the two thresholds are partly dependent on the input image, it may not be appropriate to uniformly set two fixed thresholds. In this study, the Canny method was implemented using MATALB™ software (Mathworks, Inc.) to generate adaptive double thresholds for each SST image. Before performing the edge detection, the function first generates a gradient magnitude histogram for an image. The upper threshold is defined as the 70th percentile of this histogram, then the multiplication of the upper threshold and a fixed threshold ratio (0.4 in this study) is regarded as the lower threshold. This approach is a variant of the Otsu threshold selection method (Otsu 1979; Huo et al. 2010), which is based on image binarisation. In this study, adaptive double thresholds generated in this way have been appropriately adjusted to make detected edges a more realistic representation of thermal front lines.

2.3.2. Cayula and Cornillon (1992) SIED Method

The basic principle of the Cayula and Cornillon SIED algorithm is to define edges as the pixel chain that separate two populations of image pixels that follow a bimodal histogram distribution (Wall et al. 2008). The strength of an edge is defined as the difference between the two modes of the bimodal distribution. The distance between the two modes can also be used to define the strength of an edge due to the positive relationship between the distance and the difference in the bimodal distribution. Likewise, in oceanographic research, the SIED algorithm defines thermal fronts as the thin regions that separate two water populations with relatively uniform temperature (Lekouara 2013).

The Cayula and Cornillon SIED algorithm applied in this study is basically similar to the original SIED algorithm using default parameter settings (Roberts et al. 2010). As in the Canny method, it is essential to minimise the influence of noise before edge detection. The SIED algorithm achieves this with a 2-D median filter which smooths an image with a sliding square window (filter window) of a specific size. In such a window, the value of the central pixel is replaced by the median value of the values of all the pixels in the current window. The sliding window advances across the image one pixel at a time. In this study, we median-filtered the SST images using the default 3 × 3 moving window. Second, the histogram algorithm is applied. The histogram algorithm finds a bimodal histogram distribution within a moving square window (histogram window) of a specific size. The original SIED algorithm uses a window size of 32 × 32 pixels, and the window is set to advance across 16 pixels at one time. The algorithm checks the window for a bimodal distribution in the pixel values (SST) every time the window moves. If there is a bimodal distribution in the current window, the mean values of the two populations (two water masses) will be computed. The difference between the mean values is compared with a given detection threshold. If the difference is larger than this threshold, the algorithm will conclude that there is an edge in the current window and determine the optimal value (SST) that separates the two populations. In this study, the detection threshold was set to 0.3, which indicates a minimum temperature difference of 0.3 °C.

Third, a spatial cohesion algorithm is applied in order to further verify whether the pixels of the two populations are sufficiently spatially separated, and remove noise arising from clouds and artefacts processed by satellite sensors. The presence of the two populations is initially verified by the operation above. Ideally, pixels of the same population should distribute compactly near a fixed location in the window if there is an edge. However, noisy data (i.e. clouds and satellite sensors processing artefacts) may also form populations in some histogram windows. This algorithm consists of two parts. There is a cohesion coefficient in each part to judge the level of cohesion of each of the histogram windows. The first part checks the cohesion of each population by itself. According to Cayula and Cornillon (1992), the optimal cohesion coefficients for a 32 × 32 histogram window is 0.90. The second part checks the cohesion of both populations at the same time. For this part, the optimal cohesion coefficient for a 32 × 32 histogram window given by Cayula and Cornillon (1992) is 0.92. In each part, cohesion values of the histogram windows above the cohesion coefficient are regarded as high cohesion values and represent two well-separated populations. Those windows with cohesion values below the coefficient will be filtered out because they are regarded as noisy windows. In this study, we used the same optimal cohesion coefficients (0.90, 0.92) to match our 32 × 32 histogram window. For comparing with the Canny method, fronts were also thinned to the width of one pixel.

The Cayula and Cornillon (1992) SIED Algorithm in this study was applied by using the Marine Geospatial Ecology Tools (MGET) package (Cayula & Cornillon 1992; Roberts et al. 2010) in ArcGIS (Environmental Systems Research Institute/ESRI™).

2.4. Frontal Analysis

Each frontal map contains many pixels, including those with fronts and those without fronts. For each map, frontal density (FD) was calculated as the number of frontal pixels over the total number of image pixels.

Secondly, for the analysis of frontal probability, we calculated the probability of frontal encounter (PFE), defined in Breaker et al. (2005). In different frontal maps, pixels were regarded as either frontal pixels or a non-frontal pixel. Within a certain number of frontal maps, we took the number of times a particular pixel was recognised as a frontal pixel by an edge detection algorithm and divided this value by the number of times that the pixel was a non-frontal pixel, yielding a PFE value. We produced around 60 AVHRR frontal maps and 46 MODIS frontal maps for each year. Therefore, an annual PFE image was produced by using all of the 60 AVHRR frontal maps or 46 MODIS frontal maps. Also, a monthly PFE image was produced by using 5 (=60/12 months) AVHRR images or 4 (≈46/12 months) MODIS images. An average of the PFE images was also taken to calculate corresponding annual and monthly PFE values.

Finally, we applied a modified Mann-Kendall (MMK) test to all of our time series to statistically assess if there was a monotonic trend in the frontal density and probability over time. The MMK test used in this study is based on the original Mann-Kendall test with an addition of the Yue and Wang (2004) variance correction approach, which addresses the issue of serial correlation in trend analysis. This part was achieved by using 'mmky1lag' function in CRAN-R package 'modifiedmk' (Patakamuri & O'Brien 2019).

Chapter 3 Results

3.1. Analysis of SST data

To accurately assess the performance of the frontal detection algorithms, it was necessary to evaluate the data quality of the two datasets (AVHRR/MODIS). This was achieved by computing the proportion of pixels with valid SST data in each of the SST images for each year. The test results of each dataset over each study region are shown in Figure 3.1, in the form of annual mean data quality. Data quality can reflect the reliability of subsequent results to a certain extent. We set the standard at 0.5 to distinguish between high (>0.5) and low (<0.5) data-quality years. The results of the high-quality data years are considered highly reliable in the subsequent sections of the results. Figure 3.2 shows the comparison between high- and low-quality AVHRR SST images. It can be seen in the image of 2001 that there is a large blank area due to missing data. It is not possible for frontal detection algorithms to detect fronts in areas with missing data. Therefore, according to the description of FD and PFE above, fewer detected fronts due to missing data will result in lower FD and PFE (see section 2.4).

According to the test results (see Figure 3.1a and 3.1b), for both study regions, there is an apparent poor data quality period (data quality below 0.5) between 2001 and 2005 for the AVHRR data. Although the data quality of the AVHRR data in 2003 shows a value above 0.5, poor data coverage in 2001, 2002, 2004 and 2005 will have to be treated with caution when interpreting the remaining results. In addition, poor data coverage was evident in the SW study region in 1993, 1994 and 2017 (see Figure 3.1b). These years of low-quality data will lead to a significantly low FD and PFE values. Compared with the AVHRR data, the assessment of the MODIS data quality (see Figure 3.1c and 3.1d) show absolutely higher data quality (over 0.8 data quality) during the whole time period between 2003 and 2018.

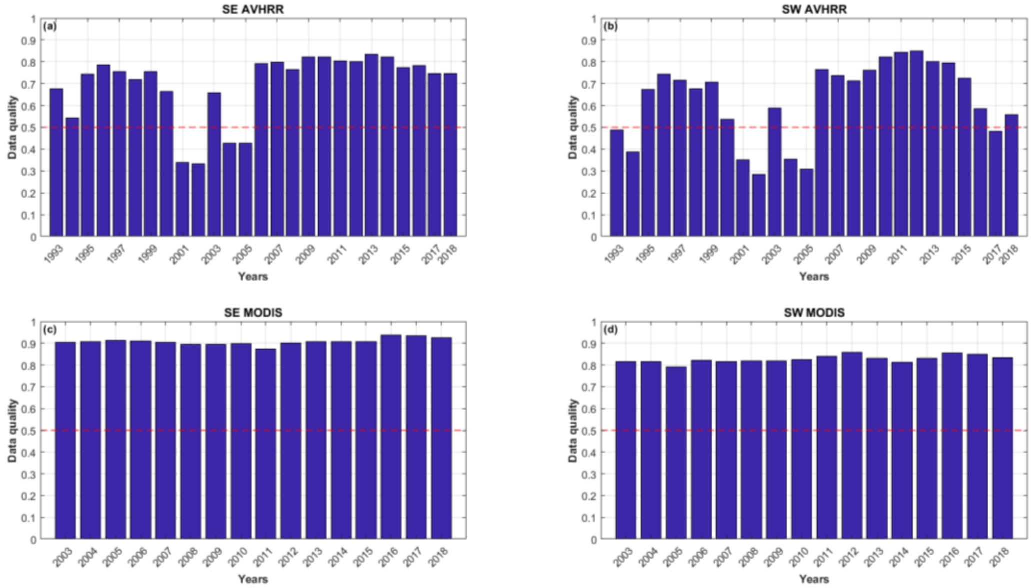

Figure 3.1 Annual average data quality of SST datasets used in this study for the South East (SE) and South West (SW) study regions for Advanced Very-High-Resolution Radiometer (AVHRR) and Moderate Resolution Imaging Spectroradiometer (MODIS) datasets.

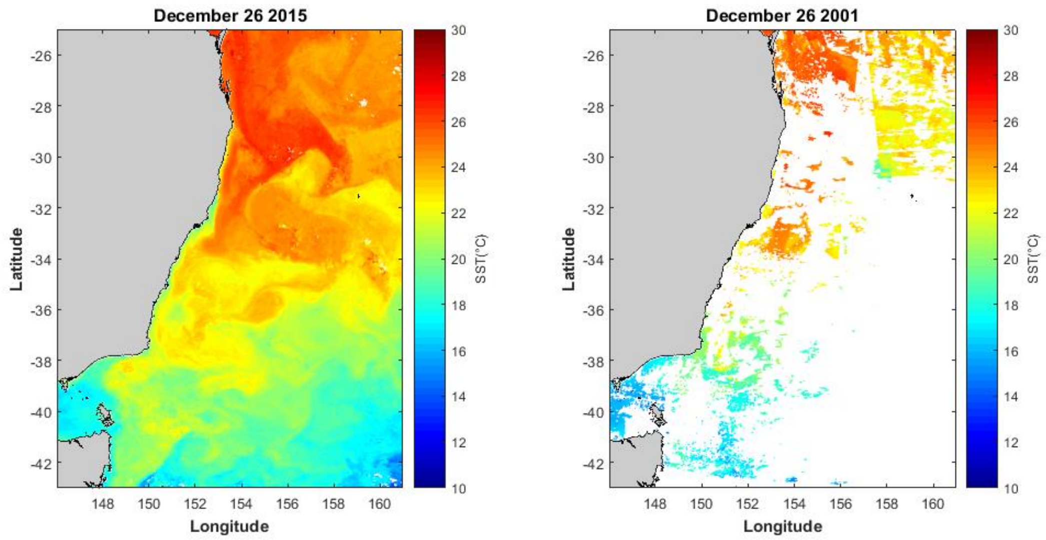

Figure 3.2 Examples of high and low data-quality SST images within the Advanced Very-High-Resolution Radiometer (AVHRR) dataset.

3.2. Analysis of the two frontal detection methods (Aim 1)

3.2.1. Adaptive Canny algorithm

The Adaptive Canny gradient-based algorithm was applied to both the

AVHRR and MODIS SST data over each study region (SE/SW). In order to see the influence of the spatial resolution of the data on edge detection, some SST images with clear fronts are shown in Figure 3.3. Figure 3.3 includes the AVHRR SST images on December 26, 2015. Fronts (black lines in Figure 3.3) were detected with the Canny method. In the following paragraphs, an SST image with fronts will be referred to as a frontal map. For comparison, frontal maps on the same date from the MODIS SST data are shown in Figure 3.4. Areas inside the red and white boxes will be used to make comparisons across algorithms and datasets.

The spatial resolution of the SST data has a significant impact on the Canny method. It is clear by comparing Figure 3.3 and Figure 3.4 that the Canny method generates thinner fronts when applied to the higher-resolution AVHRR SST data (1.1×1.1 km) compared with the MODIS SST data (4×4 km). This is expected because the Canny method suppresses edges to one-pixel width (Canny 1986). This width is defined by the spatial resolution of the input datasets. Higher-resolution data corresponds to more and smaller data pixels when displayed on an image, and further determines a thinner front width. In addition, the spatial resolution also determines the effectiveness of the algorithm to detect small-scale fronts. For instance, based on the AVHRR data, there are obvious and dense front patterns over the southwest part of the SE study region (near Furneaux Group and Tasmania) (inside the red box in Figure 3.3a). However, fewer fronts can be found in the same area in Figure 3.4. It is also worth noting that lower-quality SST data does have an effect on the Canny method. According to Figure 3.4b, there is a large area of missing SST data over the southern part of the SW study region (inside the white box), where a few fronts were detected.

3.2.2. Cayula and Cornillon SIED algorithm

To make a comparison with the Canny method, the SIED method was also applied to the same SST images from December 26, 2015. The frontal maps are shown in Figure 3.5 (AVHRR) and Figure 3.6 (MODIS). Because the SIED method in the MGET package also suppresses edges to one-pixel width (Cayula & Cornillon 1992; Roberts et al. 2010), thinner fronts can also be found in the

AVHRR frontal maps compared to the MODIS images. Although there are fewer fronts than the Canny method, it is still clear by comparing Figure 3.5 and Figure 3.6 that more fronts can be detected from high-resolution data. This indicates that the SIED method is also affected by the spatial resolution of input data.

3.2.3. Algorithm Comparison

Obviously, the performance of the two methods (Canny/SIED) varies with datasets. By comparing Figure 3.3 (AVHRR Canny) and Figure 3.5 (AVHRR SIED), the Canny method detected more fronts than the SIED method. This can also be concluded by comparing the MODIS images (see Figure 3.4 and 3.6). The difference between the two methods is also reflected in front detection near areas with poor data coverage. This can be found in the comparison between Figure 3.4b and 3.6b (area in the white boxes). Despite the obvious effect of missing data on front detection, the SIED method appears to perform better while detecting fronts in the low-quality SST data. The performance of the Canny method is obviously affected by data missing.

The difference between the two algorithms is also reflected in their PFE trends. Since the SIED method is applied only to the AVHRR SST data over the SE study region, the annual PFE data of the SE study region is shown in Figure 3.7. In Figure 3.7, we mainly focus on the difference between the two methods. Trends will be discussed in further detail in Section 3.3. In Figure 3.7, firstly, the overall PFE trends of the two methods are similar. But the annual PFE data based on the SIED method is significantly lower than the Canny PFE data. This coincides with the difference in the number of detected fronts between the two algorithms as mentioned in the previous paragraph. In addition, the difference in algorithm performance when there are areas of missing data is clearly illustrated in Figure 3.7. Based on Section 3.1, we know that the data quality between 2001 and 2005 is significantly lower. In this case, the PFE data based on the Canny method during this period is apparently lower than in other years. However, the difference in the range of the PFE values calculated using the SIED algorithm between 2001 and 2005 is much less than using the Canny method. This indicates that the effect of low-quality SST data on the performance of the SIED method is less than compared with the Canny method. For comparison, the MODIS PFE derived by the Canny method is also shown in Figure 3.7. Regardless of the potential issues with data coverage between 2001 and 2005, the PFE values from both the MODIS and AVHRR range from 0.055 to 0.075 and average 0.064.

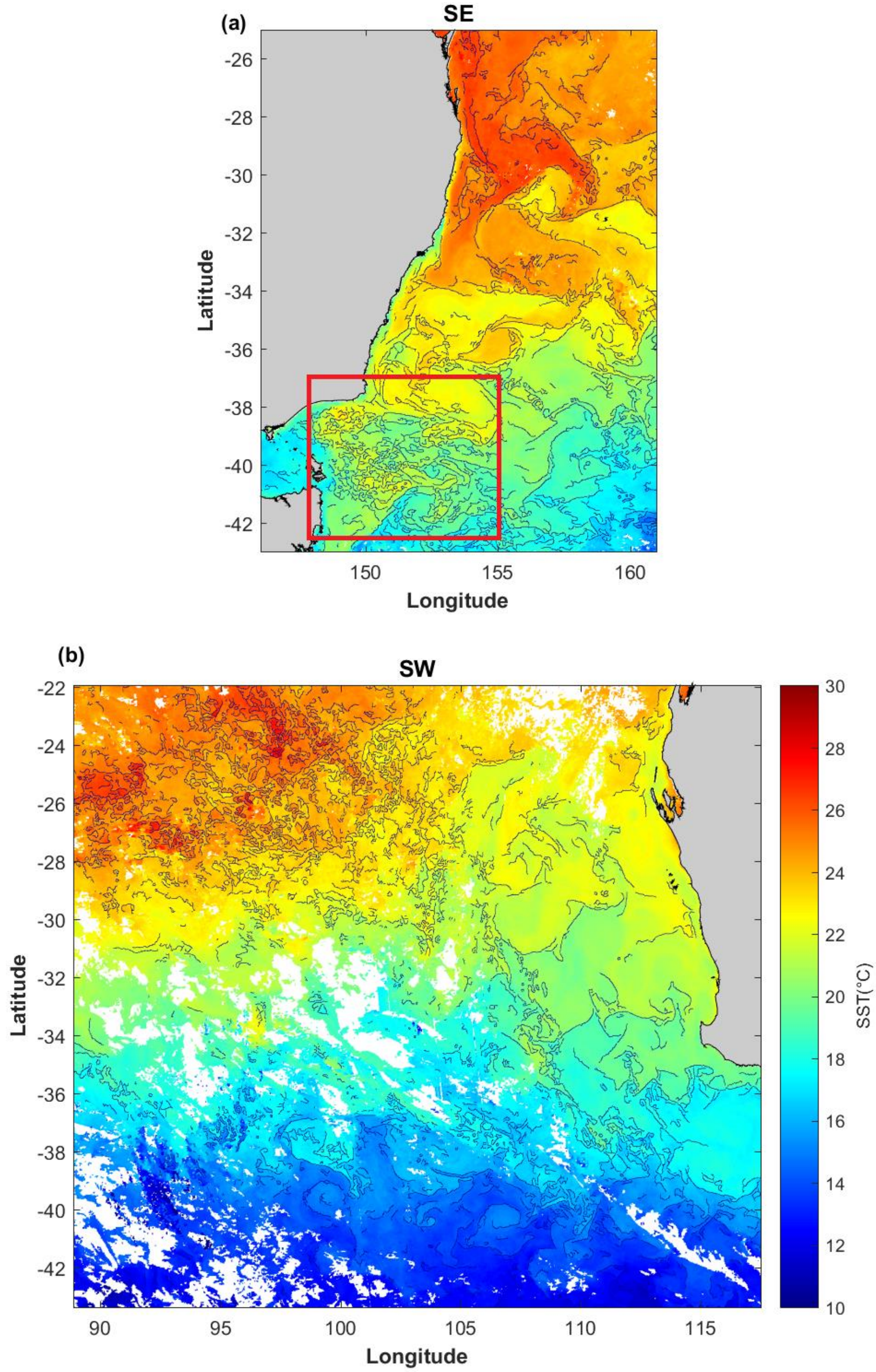

Figure 3.3 Frontal maps derived from the AVHRR SST data using the Adaptive Canny gradient-based algorithm in (a) the SE study region and (b) the SW study region. The images contain SST data from 26 December 2015 using the Advanced Very High-Resolution Radiometer (AVHRR). Black lines are thermal fronts and white areas indicate missing SST data.

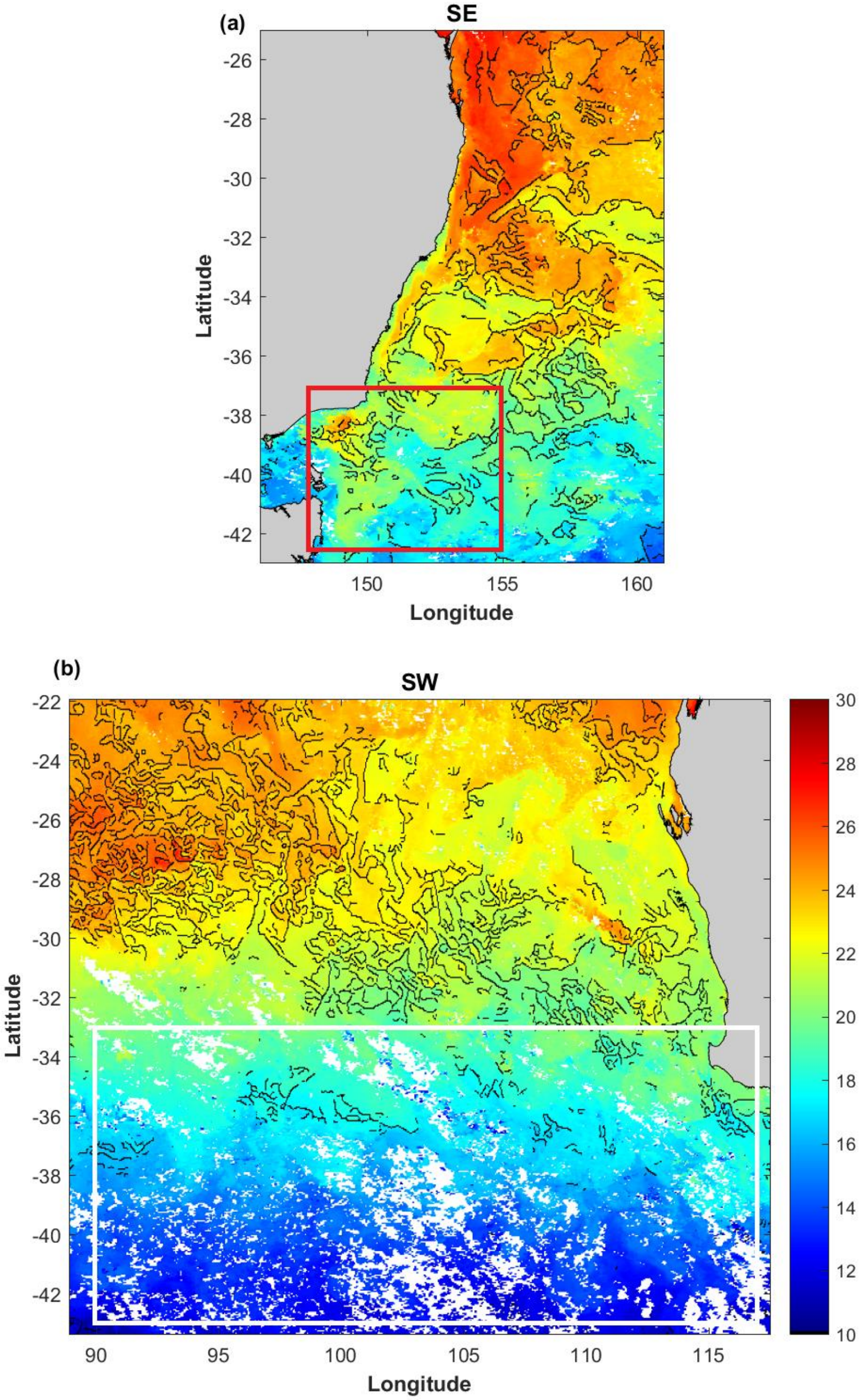

Figure 3.4 Frontal maps derived from the MODIS SST data using the Adaptive Canny gradient-based algorithm in (a) the SE study region and (b) the SW study region. The images show SST data from 26 December 2015 using the Moderate Resolution Imaging Spectroradiometer (MODIS). Black lines are thermal fronts and white areas indicate missing SST data.

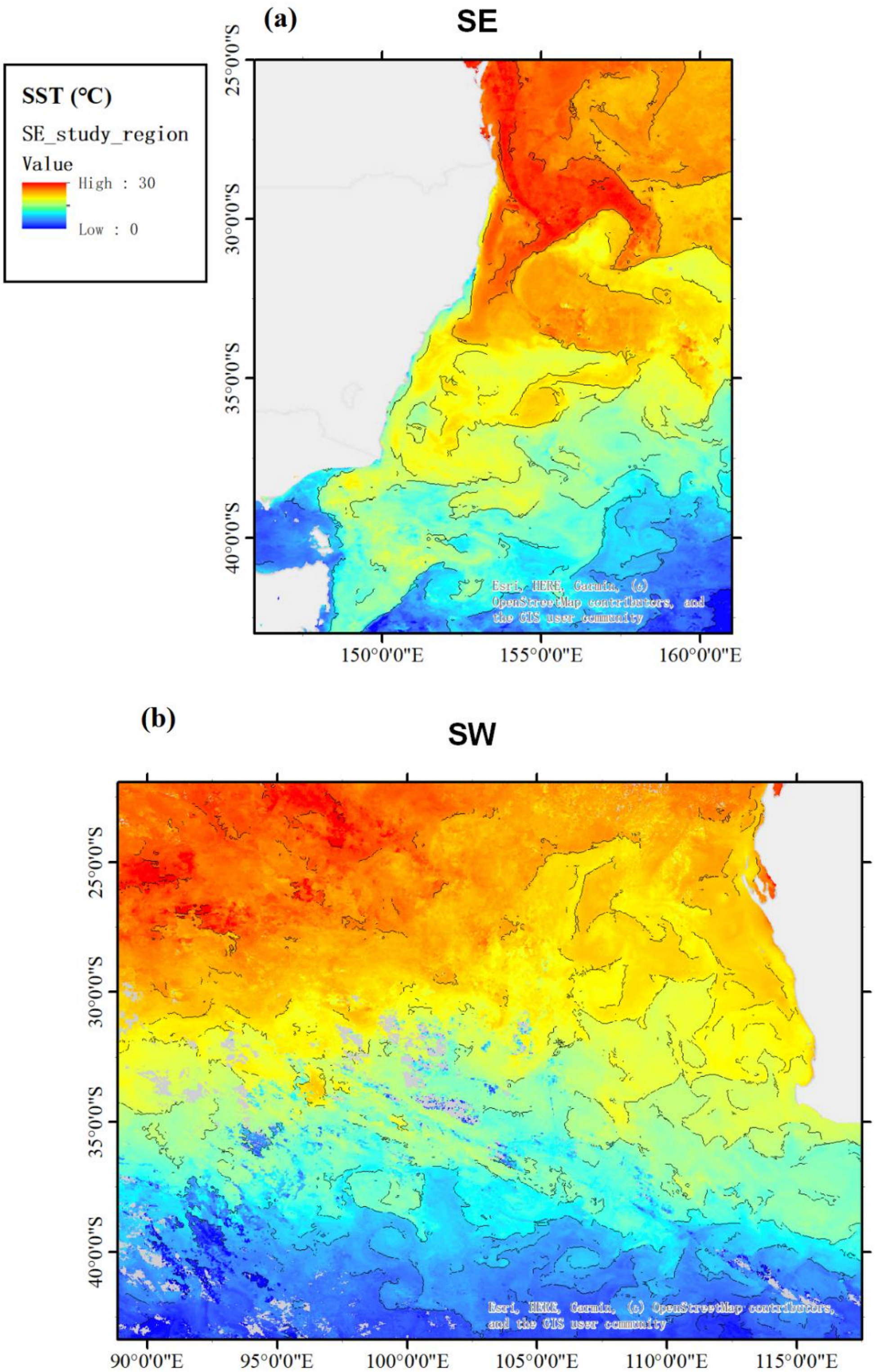

Figure 3.5 Frontal maps derived from the AVHRR SST data using the Cayula and Cornillon SIED algorithm in (a) the SE study region and (b) the SW study region. The images show SST data from 26 December 2015 using the Advanced Very High-Resolution Radiometer (AVHRR). Black lines are thermal fronts and grey areas indicate missing data.

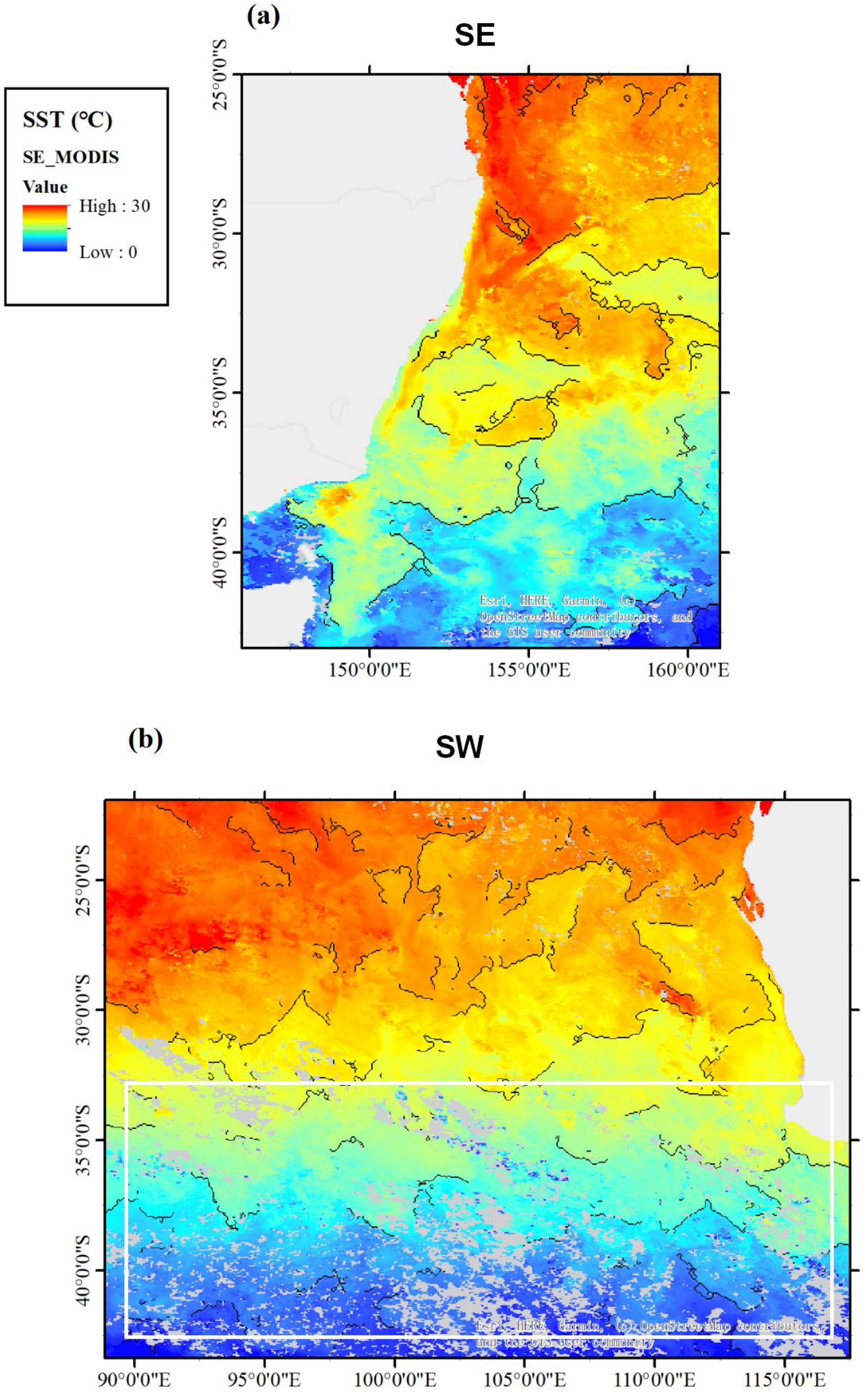

Figure 3.6 Frontal maps derived from the MODIS SST data using the Cayula and Cornillon SIED algorithm in (a) the SE study region and (b) the SW study region. The images show SST data from 26 December 2015 using the Moderate Resolution Imaging Spectroradiometer (MODIS). Black lines are thermal fronts and grey areas indicate missing data.

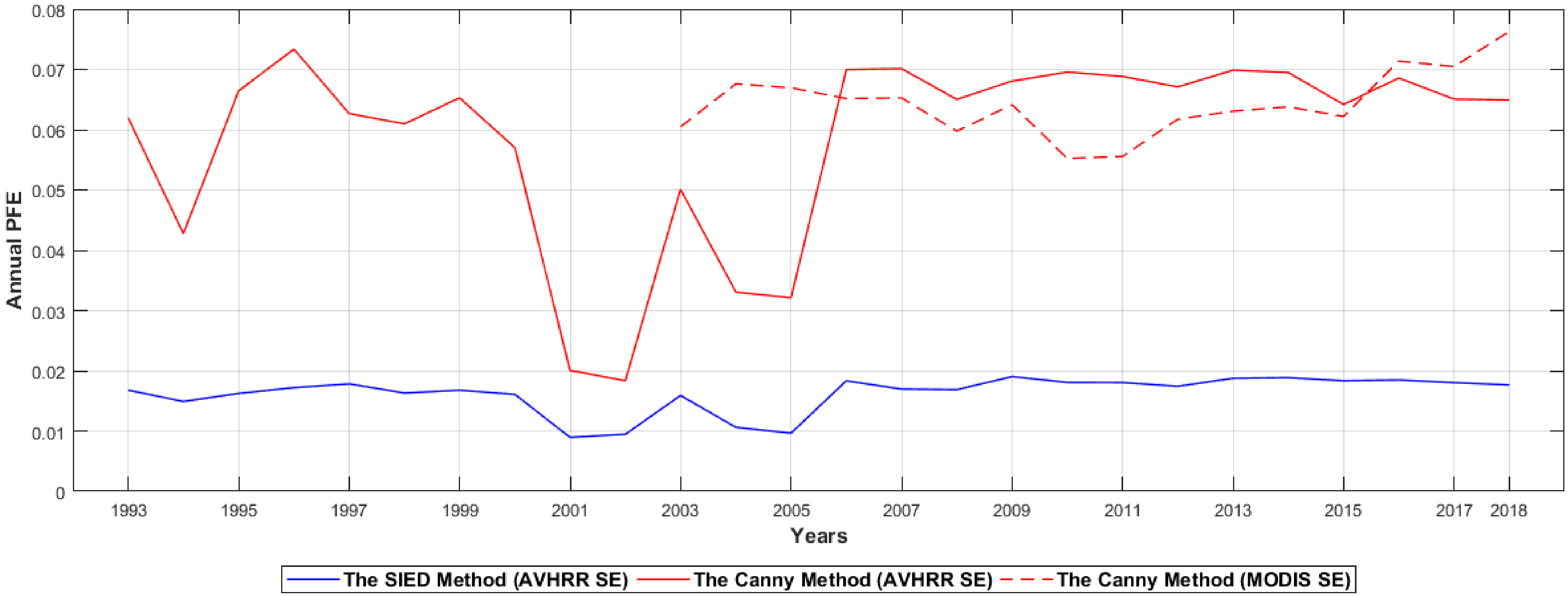

Figure 3.7 Time series of annual probability of frontal encounter (PFE) in the South East Australia (SE) study region based on different edge detection algorithms.

3.3. Trend Analysis (Aim 2)

3.3.1. AVHRR results

Based on the data quality analysis in Section 3.1, the entire 26-year study period of the AVHRR results was divided into three sub-periods: P1, P2 and P3. P1 corresponds to the period from 1993 to 2000 and P2 corresponds to the period from 2001 to 2005. P3 represents the period between 2006 and 2018. The main part of this section will pay more attention to the images and numerical results of P1 and P3 because results of P2 were affected to a large extent by a large amount of missing AVHRR SST data.

According to the definition of PFE above, the high PFE value of a pixel corresponds to high frontal probability, which means that frontal activity frequently occurs at a particular pixel location. In the following PFE images, areas of relatively high PFEs were represented by bright/warm colours while those with low PFEs are represented by cooler colours.

Figure 3.8 shows the 26 annual PFE images of the SE study region. Fronts in these images were derived from the AVHRR data using the Adaptive Canny gradient-based algorithm. Overall, the images of 2001, 2002, 2004 and 2005 show much lower frontal activity than those of other years due to low-quality AVHRR SST data (see Section 3.1). In terms of spatial distribution, frontal activity is higher near the coastline compared to offshore. Compared to the P1 period, frontal activity of the P3 period seems to be higher. It also appears that frontal activity has increased in P3 over the years. Overall, the frontal activity between 1993 and 2018 appears to follow a gently rising trend.

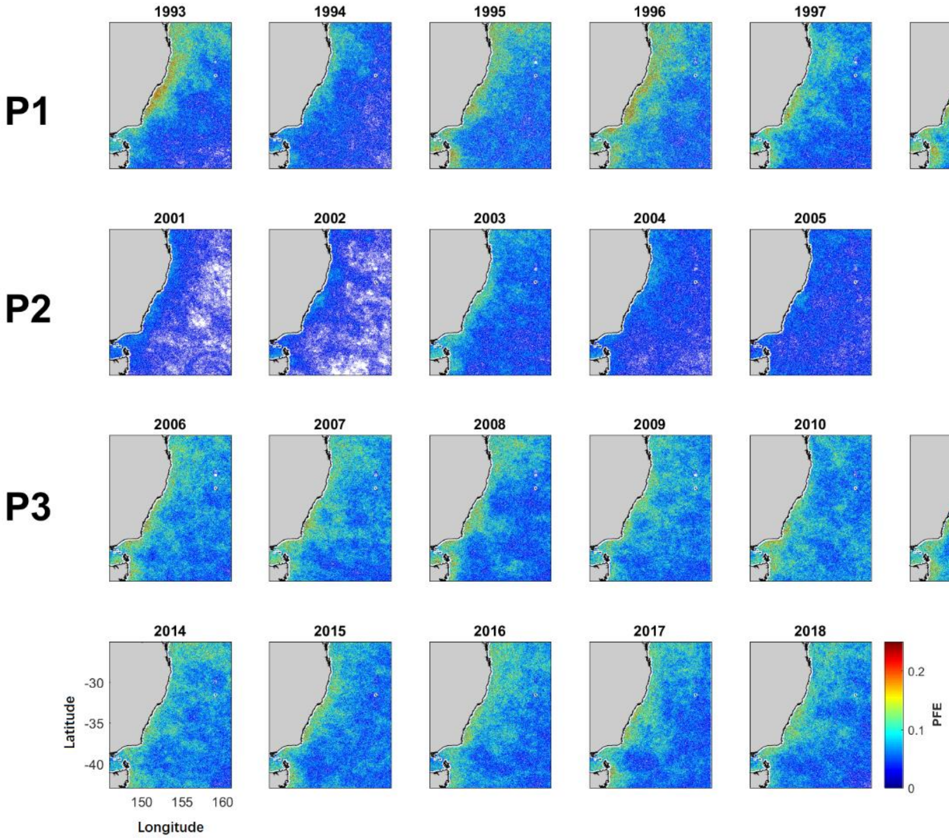

Figure 3.8 Annual probability of frontal encounter (PFE) images of the South East Australia (SE) study region derived from the Advanced Very High-Resolution Radiometer (AVHRR) data. Thermal front detection is based on the Adaptive Canny Gradient-based Algorithm. P1 is the period of 1993 to 2000, P2 is the period of 2001 to 2005 and P3 is between 2006 to 2018. White areas indicate a PFE of 0.

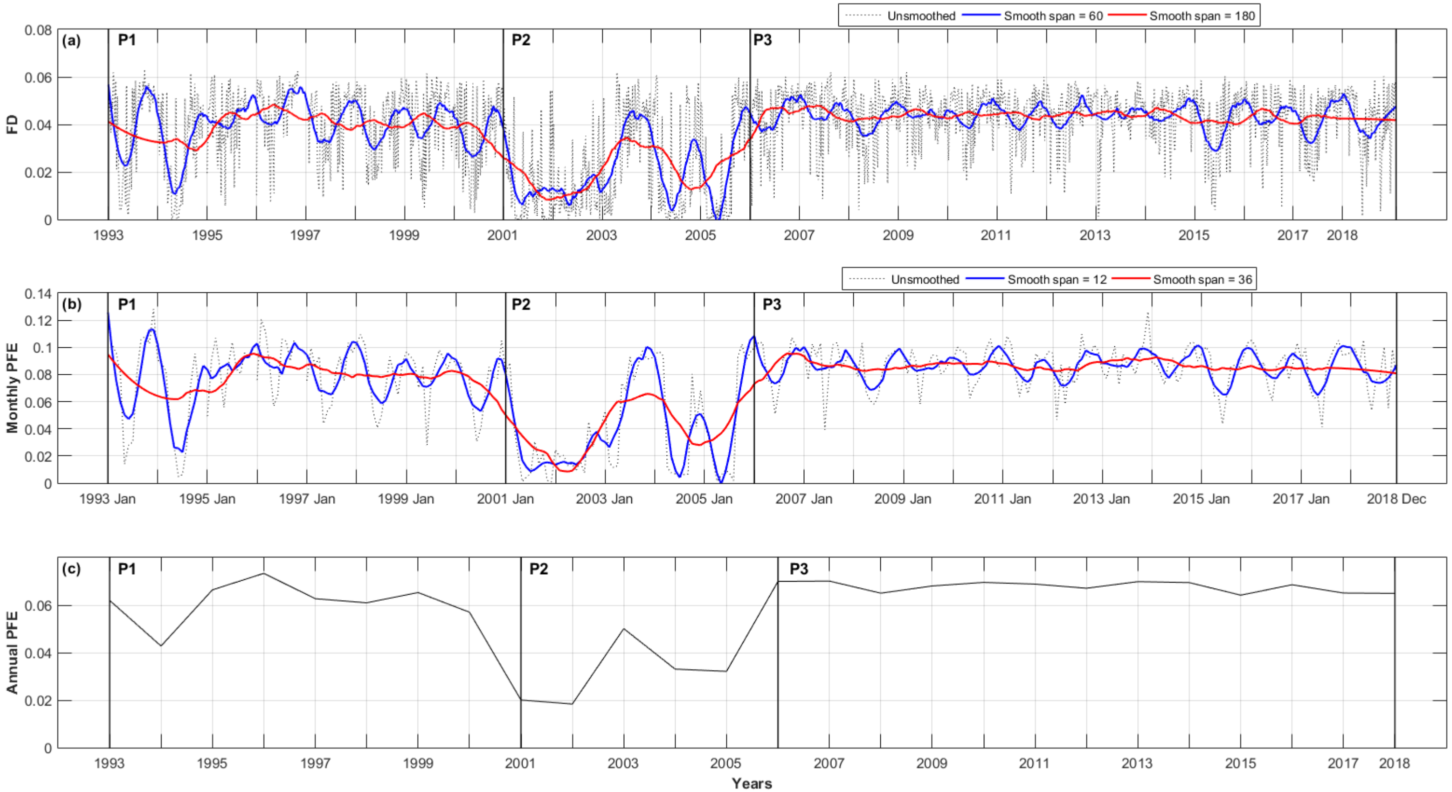

Figure 3.9 Time series of (a) the 6-day average FD, (b) the monthly average PFE and (c) the annual average PFE for the SE study region using the Advanced Very High-Resolution Radiometer (AVHRR) SST data. Thermal fronts were detected by the Adaptive Canny Gradient-based Algorithm. FD is frontal density. PFE is the probability of frontal encounter. P1 denotes the period between 1993 to 2000, P2 between 2001 to 2005 and P3 between 2006 to 2018.

Table 3.1 Comparison of the mean values of the smoothed FD (red curve in Figure 3.9a), smoothed monthly PFE (red curve in Figure 3.9b) and annual PFE (Figure 3.9c) in P1 and P3 (results from AVHRR SST data of the South East Australia (SE) study region). P1 is between 1993 to 2000 and P3 is the period between 2006 to 2018.

Frontal Product	P1	P3	P3-P1
FD (smoothed)	0.0391	0.0435↑	+0.0044
Monthly PFE (smoothed)	0.0782	0.0861↑	+0.0079
Annual PFE	0.0613	0.0678↑	+0.0065

↑, the larger value between the two values of P1 and P3; FD, frontal density; PFE, probability of frontal encounter; P1, period from 1993 to 2000; P3, period from 2006 to 2018.

In order to analyse the trends of frontal activity, the corresponding time series of (a) the 6-day average FD, (b) the monthly average PFE and (c) the annual average PFE are shown in Figure 3.9. In Figure 3.9a and 3.9b, in order to show the seasonal variability and overall trend of FD and monthly PFE, the original curves were smoothed by applying the appropriate smoothing windows. Smoothing was done using a moving average filter known as the Savizky-Golay filter (Orfanidis 1996). Unsmoothed raw FD and monthly PFE data are displayed as dotted lines. Smoothing is based on two different smoothing windows. To represent the seasonal variability of FD, we smoothed its raw data to represent annual trends (blue curve in Figure 3.9a). This corresponds to a smooth span of 60 because there are 60 FD values in a year for the 6-day average AVHRR data. The red curve representing the overall FD trend was smoothed in a smooth span of 180 (see Figure 3.9a). Monthly PFE values were smoothed to represent seasonal variability (see Figure 3.9b). Seasonal variability of FD and monthly PFE can also be found in Figure 3.9a and 3.9b (blue curves). Roughly, both FD and monthly PFE have significant decreasing trends in the first half of each year and increasing trends in the second half. This means that frontal activity reached a trough from June to August (winter) and a peak from November to January (summer).

Despite the seasonal variation, the FD and PFEs (monthly PFE and annual PFE), frontal activity follows a gentle increasing slope (see Figure 3.9c). This trend is not significant in Figure 3.9, but it can still be captured from the mean FD and PFEs (see Table 3.2) particularly for the P1 and P3 periods. Compared to P1, the mean FD and PFEs of P3 show a slight increase. Another point worth noting in Figure 3.9c is that the trend of annual PFE has a relatively significant fluctuation between 1994 and 1996 (see Figure 3.9b). The red smoothed curves in Figure 3.9a and 3.9b also show the same fluctuation pattern during this period. This can be attributed to the relatively poor data quality (~0.5) in 1994 (see Figure 3.1a).

For the SW study region, the 26 annual PFE images are shown in Figure 3.10. Because this study region covers a larger area and extends to further into the Indian Ocean, the difference between coastal and ocean frontal activity is much clearer. According to the data quality analysis in Section 3.2.1, in the SW study region, the PFE images of 2001, 2002, 2004 and 2005 also show a lower frontal activity. In addition, the frontal probability between 2015 and 2018 decreases. This is also due to low-quality SST data. Except for images affected by low-quality SST data in P2, the overall trend of frontal activity over the SW study region seems stable during P1 and P3.

Figure 3.11 shows the trends in (a) the 6-day average FD, (b) the monthly average PFE and (c) the annual average PFE for the SW hotspot region. The FD and monthly PFE were also smoothed in the same way as in Figure 3.9. The blue curves in Figure 3.11a and 3.11b also show seasonal variability in the FD and monthly PFE, peaking in summer and reaching a trough during the winter months. This is consistent with the conclusion drawn from the analysis of the SE study region above.

As seen in the imagery of Figure 3.10, the trends of frontal probability for the SW study region also seems stable in Figure 3.11. But according to the mean data shown in Table 3.2, it can be found that the trend is also gently increasing. By comparing Table 3.2 with Table 3.1, the overall trends of PFEs for SW appears to be flatter than for the SE region. It is noticed that there are obvious fluctuations in trends of FD and PFEs in the periods of 1993-1995 and 2015-2018. Based on Section 3.1, we know that the SST data are of low quality in 1993, 1994 and 2017. In addition, according to Figure 3.6b, during the two periods, trends of FD and PFEs follow a similar pattern to data quality. Therefore, these fluctuations may be largely influenced by missing data.

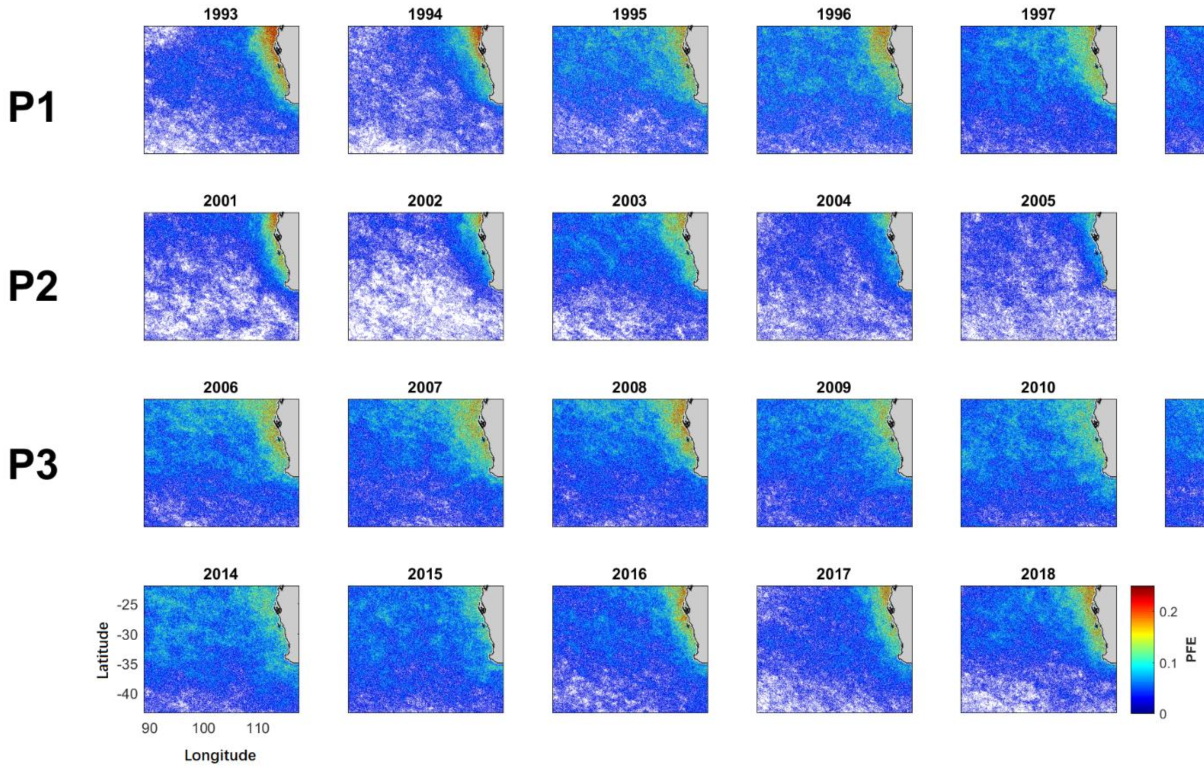

Figure 3.10 Annual probability of frontal encounter (PFE) images of the South West Australia (SW) study region derived from the Advanced Very High-Resolution Radiometer (AVHRR) data. Thermal front detection is based on the Adaptive Canny Gradient-based Algorithm. P1 is the period of 1993 to 2000, P2 is the period of 2001 to 2005 and P3 is between 2006 to 2018. White areas indicate a PFE of 0.

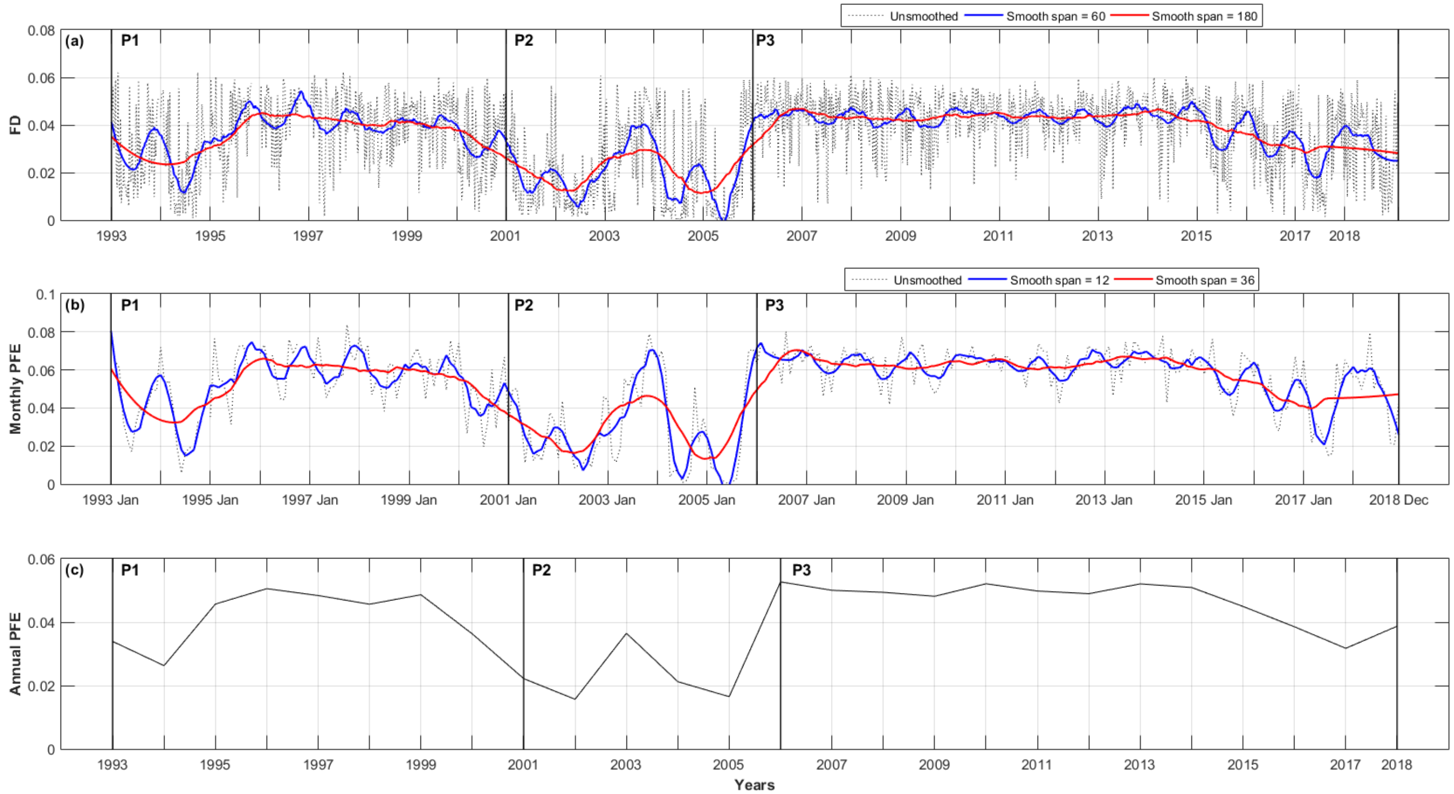

Figure 3.11 Time series of (a) 6-day average FD, (b) monthly average PFE and (c) annual average PFE for the SW study region using the Advanced Very High-Resolution Radiometer (AVHRR) SST data. Thermal front detection was based on the Adaptive Canny Gradient-based Algorithm. FD is frontal density. PFE is the probability of frontal encounter. P1 denotes the period between 1993 to 2000, P2 between 2001 to 2005 and P3 between 2006 to 2018;

Table 3.2 Comparison of the mean values of the smoothed FD (red curve in Figure 3.11a), smoothed monthly PFE (red curve in Figure 3.11b) and annual PFE (Figure 3.11c) in P1 and P3 (results from AVHRR SST data of the South West Australia (SW) study region). P1, Period of 1993 to 2000; P3, Period of 2006 to 2018;

Frontal Product	P1	P3	P3-P1
FD (smoothed)	0.0361	0.0400↑	+0.0039
Monthly PFE (smoothed)	0.0531	0.0588↑	+0.0057
Annual PFE	0.0419	0.0468↑	+0.0049

↑, the larger value between the two values of P1 and P3; FD, frontal density; PFE, probability of frontal encounter; P1, period from 1993 to 2000; P3, period from 2006 to 2018.

3.3.2. MODIS results

Based on the analysis in Section 3.1, results derived from high-quality MODIS data potentially provide a more accurate assessment of trends of frontal activity in these hotspots. Similar to the analysis of the AVHRR results, let us first pay attention to the PFE images over the years. Figure 3.12 shows the 16 annual PFE images of the SE study region derived from the MODIS data using the Adaptive Canny gradient-based algorithm. Each image in Figure 3.12 shows areas of higher frontal activity near the coastline between 25° S and 35° S. The PFE or frontal activity during most years is similar except in 2004, 2010 and 2018. Large areas of relatively high PFE appear during 2004 and 2018. 2010 is a year that has a relatively lower frontal activity compared to other years. Compared with images derived from AVHRR data (see Figure 3.8), the MODIS PFE images show greater differences in frontal activity between low-latitude and high-latitude areas; higher in the lower latitudes and lower in the higher latitudes. For some years such as 2018, the AVHRR and MODIS images show quite different patterns. In addition, based on the high-quality MODIS SST data, images of apparent low frontal activity (2004 and 2005) of AVHRR (see Figure 3.9) are not evident in the MODIS data (see Figure 3.12).

In the same way, time series of (a) the 8-day average FD, (b) the monthly average PFE and (c) the annual average PFE for the SE region are shown in Figure 3.13. In Figure 3.13a, for seasonal variability, the smoothing window of FD was adjusted as there are a total of 46 FD values in a year for the 8-day average MODIS data. Another smooth span for FD was also adjusted accordingly to show the overall trend of FD. Based on the blue curves in Figure 3.13a and 3.13b, seasonal variability in FD and monthly PFE can still be found. There is high frontal activity in summer and low activity in the winter. This is consistent with the results of the AVHRR data. In addition, the overall trends of frontal density and probability during the whole time period of the MODIS data (from 2003 to 2018) follow a gently rising trend (see Figure 3.13). This increase is more obvious compared with the trends in the AVHRR data (see Figure 3.9). According to Figure 3.13c, between 2003 and 2018, the annual PFE increase from ~0.060 to ~0.075. It is also worth noting that there appears to be a decrease in FD and PFEs from 2006 and a trough in 2010. This is particularly evident in the curve of the annual PFE (see Figure 3.13c). The value of the 2010 annual PFE is the lowest of all 16 years (~ 0.055). Since then, the trends of FD and PFEs increase, reaching a peak in 2018 (annual PFE ~0.077). During this period, the upward trends flattened twice; once in 2015 and then again in 2017 (see Figure 3.13). This can also be seen in the annual PFE curve (see Figure 3.13c).

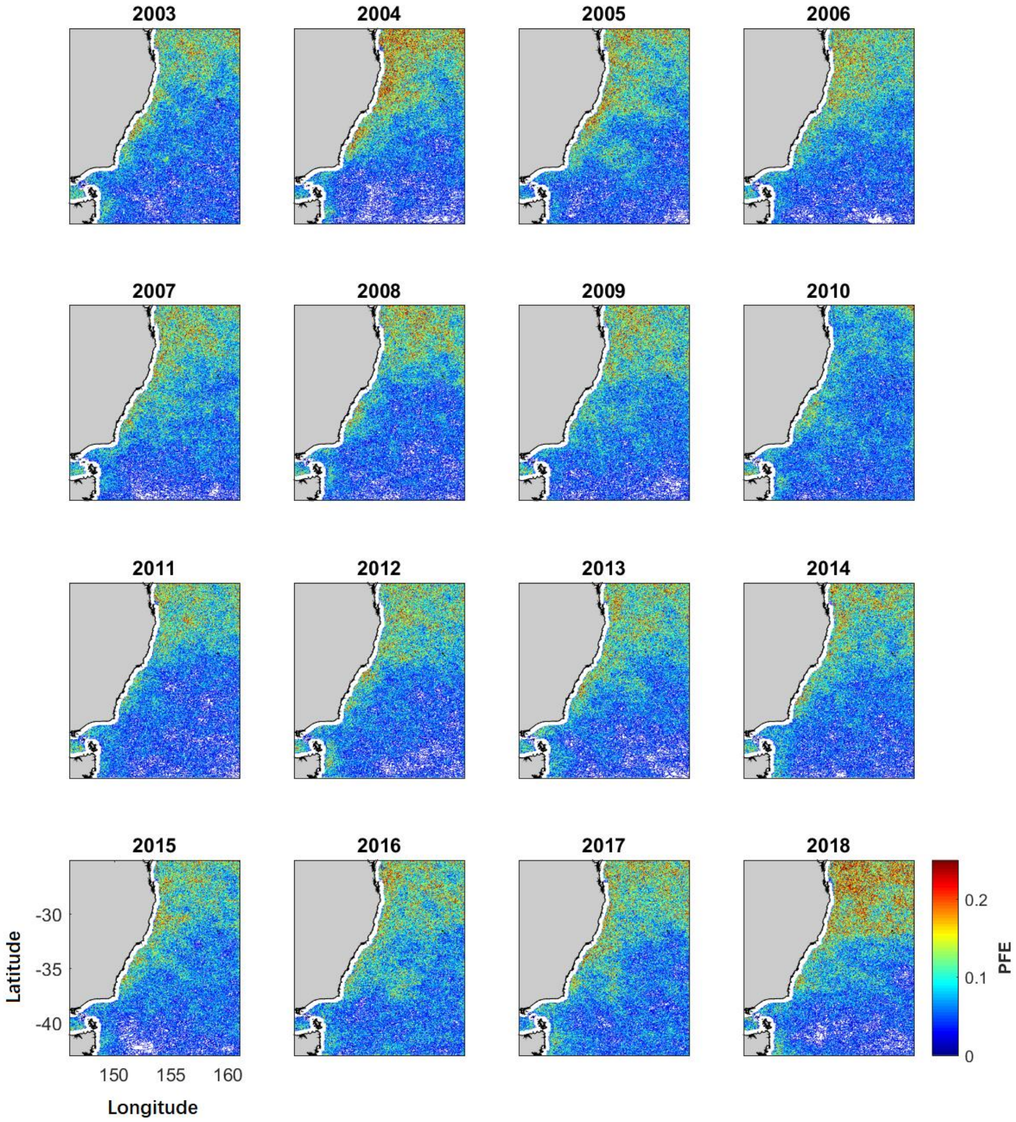

Figure 3.12 Annual probability of frontal encounter (PFE) images of the South East Australia (SE) study region derived from the Moderate Resolution Imaging Spectroradiometer (MODIS) data. Thermal front detection is based on the Adaptive Canny Gradient-based Algorithm. P1 is the period of 1993 to 2000, P2 is the period of 2001 to 2005 and P3 is between 2006 to 2018. White areas indicate a PFE of 0.

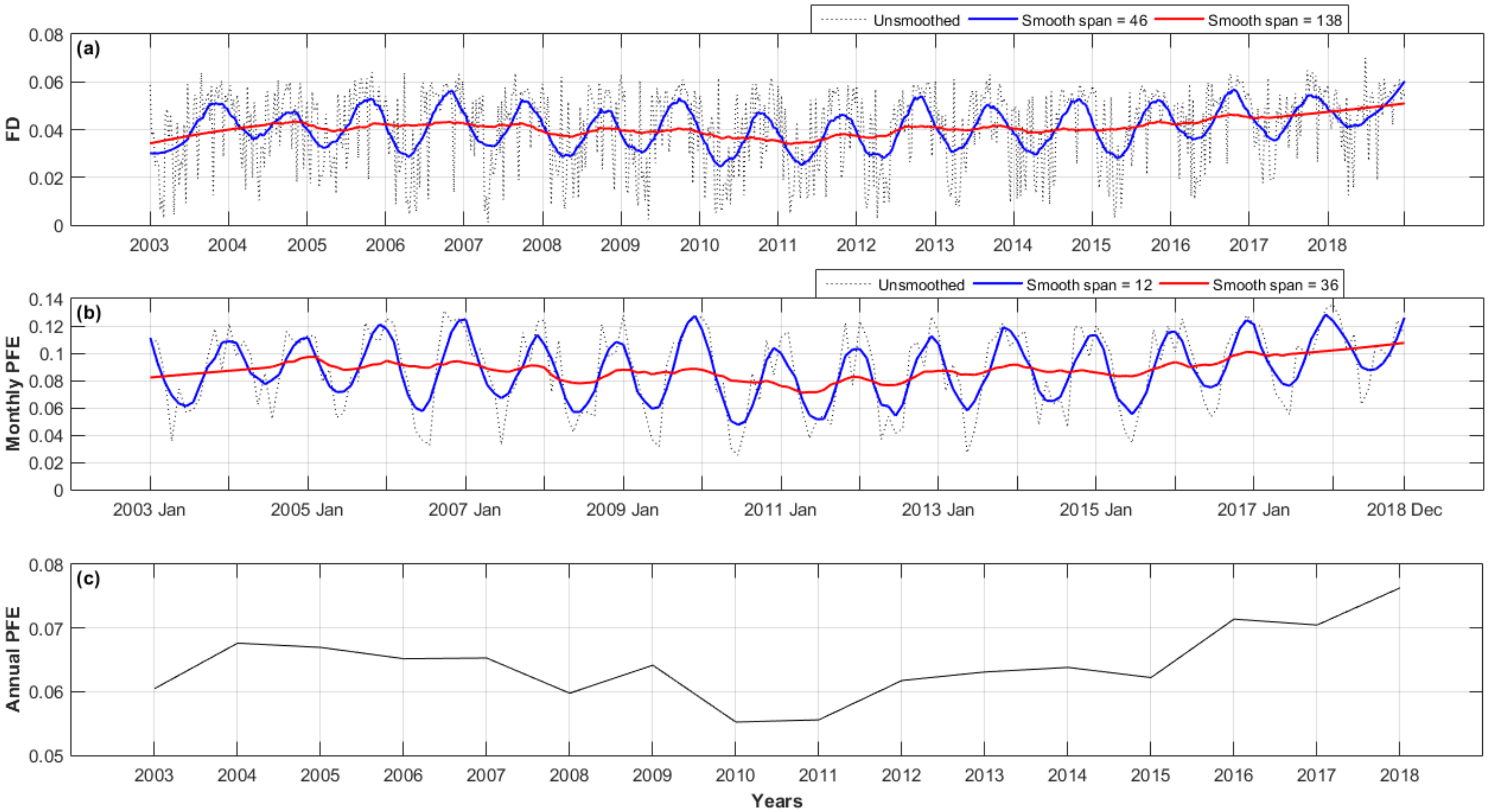

Figure 3.13 Time series of (a) the 6-day average FD, (b) the monthly average PFE and (c) the annual average PFE for the SE study region using the Moderate Resolution Imaging Spectroradiometer (MODIS) SST data. Thermal front detection was based on the Adaptive Canny Gradient-based Algorithm. FD is frontal density. PFE is the probability of frontal encounter

For the SW study region, the 16 annual PFE images are shown in Figure 3.14. Similar to the SE study region, images in Figure 3.12 also show a regional difference in frontal activity between low- and high-latitude areas, which is harder to see in the AVHRR PFE images in Figure 3.8. In addition, the spatial structure of frontal activity between 2003 and 2013 is largely similar with higher activity in the lower latitudes and along the coastal areas. It appears that there is a decrease in frontal activity between 2014 to 2017 over the whole SW study area. But this decrease did not seem to continue after 2017. In addition, in 2018, there is a clear gradient between areas of high and low activity at about 32°S.

Similarly, Figure 3.15 shows trends of (a) the 8-day average FD, b) the monthly average PFE and c) the annual average PFE for the SW study region. Seasonal variability in FD and monthly PFE can still be found from the blue curves in Figure 3.15a and 3.15b, reflecting a similar pattern as was found in the AVHRR data. So far, the results of two datasets (AVHRR/MODIS) over two study regions (SE/SW) have reached an agreement on the seasonal variability of FD and monthly PFE; high in summer and low in winter. In addition, based on Figure 3.15, the overall trends of frontal density and probability for SW follow the gently rising trends for the SE region. Over the course of the 16 years, the annual PFE has increased from approximately 0.044 to 0.057. Corresponding to the decreased frontal activity between 2014 and 2017 mentioned in the analysis of Figure 3.14, FD and PFEs in Figure 3.15 also decline during the same time period.

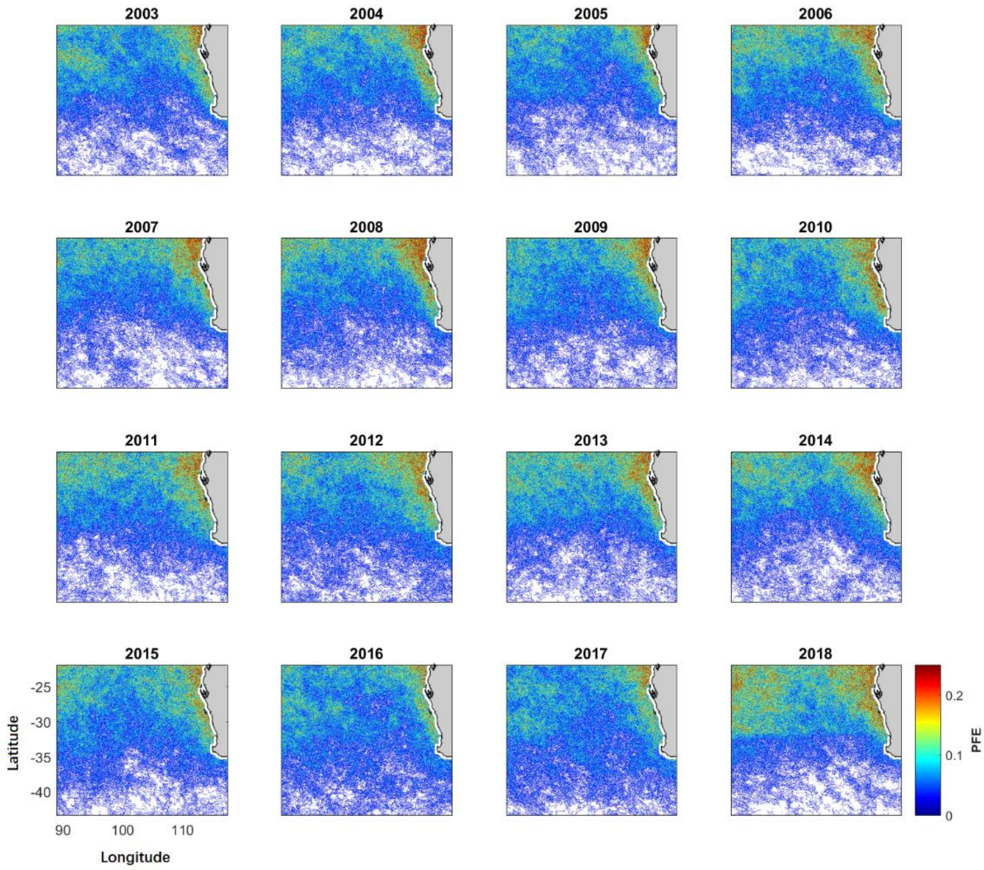

Figure 3.14 Annual probability of frontal encounter (PFE) images of the South West Australia (SW) study region derived from the Moderate Resolution Imaging Spectroradiometer (MODIS) data. Thermal front detection is based on the Adaptive Canny Gradient-based Algorithm. P1 is the period of 1993 to 2000, P2 is the period of 2001 to 2005 and P3 is between 2006 to 2018. White areas indicate a PFE of 0.

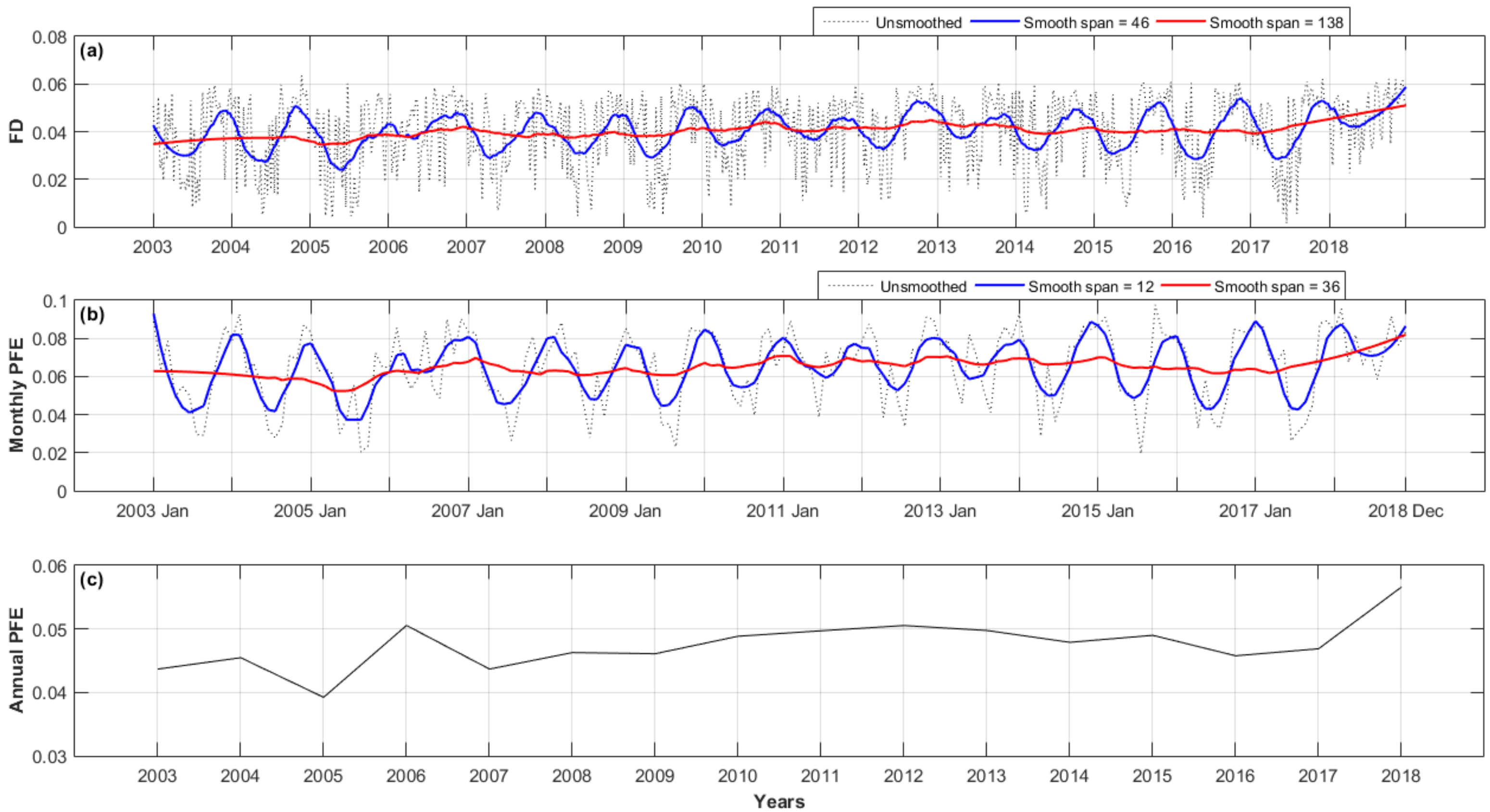

Figure 3.15 Time series of (a) the 6-day average FD, (b) the monthly average PFE and (c) the annual average PFE for the SW study region using the Moderate Resolution Imaging Spectroradiometer (MODIS) SST data. Thermal front detection was based on the Adaptive Canny Gradient-based Algorithm. FD is frontal density. PFE is the probability of frontal encounter.

3.4. Modified Mann-Kendall test (Aim 2)

Based on Section 3.2, results produced by AVHRR and MODIS all show gently increasing frontal activity over the years. To assess these trends, we applied the modified Mann-Kendal test to all of the time series of FD and PFEs. Results are shown in Table 4. First, tests for each time series provides a positive Z-value, which indicates that frontal activity does increase across the years in both hotspot regions. In addition, according to their corresponding P-values, most PFE results show that the trends are not significant. The upward trend of FD based on the Canny method is statistically significant for both the AVHRR and MODIS datasets.

Table 3.3 Results of the Modified Mann–Kendall test applied to serially correlated data. The test was applied to results from the Advanced Very-High-Resolution Radiometer (AVHRR)/Moderate Resolution Imaging Spectroradiometer (MODIS) data over the South East Australia study region (SE) and the South West Australia study region (SW), using the Cayula and Cornillon SIED algorithm (SIED)/Adaptive Canny gradient-based algorithm (Canny). APFE, the annual probability of frontal encounter; MPFE, the monthly probability of frontal encounter; FD, frontal density;

Frontal Product	Source	Time series	Region	Edge detection algorithm	Z-value	P-value
APFE	**AVHRR**	**1993-2018**	**SE**	**SIED**	**+1.73***	**0.083**
APFE	AVHRR	1993-2018	SE	Canny	+0.69	0.492
APFE	AVHRR	1993-2018	SW	Canny	+0.44	0.659
APFE	MODIS	2003-2018	SE	Canny	+0.48	0.635
APFE	**MODIS**	**2003-2018**	**SW**	**Canny**	**+2.63*****	**0.009**
MPFE	AVHRR	1993-2018	SE	Canny	+1.11	0.268
MPFE	AVHRR	1993-2018	SW	Canny	+0.73	0.468
MPFE	MODIS	2003-2018	SE	Canny	+0.63	0.528
MPFE	MODIS	2003-2018	SW	Canny	+1.37	0.168
FD	**AVHRR**	**1993-2018**	**SE**	**Canny**	**+2.92*****	**0.003**
FD	**AVHRR**	**1993-2018**	**SW**	**Canny**	**+2.17 ** **	**0.030**
FD	**MODIS**	**2003-2018**	**SE**	**Canny**	**+1.70 ***	**0.089**
FD	**MODIS**	**2003-2018**	**SW**	**Canny**	**+2.83*****	**0.005**

*, significant at a 90% confidence interval; ** significant at a 95% confidence interval; and ***, significant at a 99% confidence interval.

Chapter 4 Discussion

In comparing results between the SST products (AVHRR and MODIS) and the algorithms (Canny and SIED), this study mainly examined the differences between the performance of the two frontal detection algorithms applied to two SST products and the interannual and seasonal trends of frontal activity in marine hotspots.

4.1. Comparison between the edge detection algorithms and the SST products (Aim 1)

Firstly, the spatial resolution of the SST data influences the performance of both algorithms (Canny and SIED). Thinner and smaller-scale fronts can be detected in high-resolution SST data from AVHRR compared to the low-resolution MODIS data. This is likely due to the front-thinning process in the two algorithms that suppresses fronts to one-pixel width (Canny 1986; Cayula & Cornillon 1992; Roberts et al. 2010), with the spatial resolution of the data determining the size of imagery pixels. Higher spatial resolution corresponds to smaller pixels. Smaller frontal pixels detected by edge detection algorithms form thinner fronts. Based on this, we recommend the high-resolution AVHRR data for detecting and resolving fine-scale fronts, especially for studying nearshore coastal areas. The coarser-resolution MODIS data should be considered for exploring the overall change in fronts in areas for regional comparison.

According to the algorithm comparison, this study demonstrates that there are two differences between the Canny and the SIED methods. One of them is that the Canny method detected more fronts than SIED. A possible reason for this difference is the detecting principles of the two algorithms. The Canny method defines thermal fronts by finding strong temperature gradient in the SST field, while SIED analyses the histogram of SST values to search for evidence of two distinct temperature populations (Robinson 2010). Therefore, although the Canny method can detect more fronts, there is no doubt that the detection is sensitive to changes and may contain false detections due to the potential noise in SST data (e.g. cloud edge, processing error etc.). Holyer and Peckinpaugh (1989) also suggested that gradient-based methods were too sensitive to fine-scale features and weak gradients. As for the SIED method, histogram analysis focuses more on detecting two water masses with different properties (SST) so that it can partly filter out false fronts (Cayula & Cornillon 1992). According to the evaluation of the SIED method and the Sobel gradient-based method by Ullman and Cornillon (2000), the gradient method detects more false fronts and is less tolerant to noise than the histogram method. Based on this study, further evaluation of the Canny method in the future is also expected to draw a similar conclusion. Another important difference is that SIED performs better when processing poor-quality data. We suspect this to be due to the larger kernel box (histogram window) (32×32) applied in the SIED method compared to the Canny method (3×3 kernel box). Because the same number of missing data pixels occupy different proportions in kernel boxes of different sizes. The larger the proportion, the larger the impact of missing data on frontal detection. So a smaller kernel box makes the Canny approach more vulnerable to missing data (see Figure 3.4b). Through a further evaluation of algorithms, this might be fixed by adjusting the kernel size in future studies. Wall et al. (2008) applied the SIED method with two different kernel sizes (32×32, 16×16). Their results showed that the 16×16 kernel box can detect more fronts including some weak fronts, compared with the 32×32 kernel box.

Ground-truthing surveys will be required to further evaluate these detection methods. Currently, frontal studies just assume that frontal detection gives reasonable results, and that they are based on the data-limited ground truth validation. A visual examination of fronts drawn on satellite imagery remains the most common method for validating the effectiveness of the algorithms (Wall et al. 2008). However, based on the results of this study, inconsistencies between algorithms and datasets are evident. Further ground-truthing surveys will be able to confirm whether there is excessive detection using the Canny method or whether fronts are missed with the SIED method.

Therefore, although ground truthing is necessary to validate the results of this study, it is expensive and labour intensive. Ground truthing fronts in satellite images could involve coordination with autonomous underwater vehicle (AUV) surveys. The AUV surveys had been used by Robbins et al. (2006) to gather spatially and temporally relevant data that can be used in collaboration with satellite imagery for studying fronts associated with algal bloom dynamics. In addition, Zhang et al. (2012) developed an AUV method that allows AUV to autonomously detect and track an upwelling front and combined AUV data with SST satellite imagery to examine structure and dynamics of upwelling fronts. Based on the requirements suggested by Pereira et al. (1995), to validate the frontal detection algorithms, immediate in situ temperature data produced by AUV sensors should be combined with satellite imagery and frontal detection to evaluate the integration of results from AUV surveys and front detection algorithms. In addition, AUV surveys can also contribute to the determination of the fine-scale structure of fronts by combining AUV surveys with higher resolution satellite imagery, such as Landsat data (30 × 30m).

Both the Canny method (gradient method) and the SIED method (statistical method) can contribute to local definitions of SST fronts (Chapman et al. 2020). Evaluation and comparison of the two methods based on in situ data are still needed to judge their applicability to different conditions. Results of additional evaluations are likely to be similar to the results of the evaluation by Ullman and Cornillon (2000). They evaluated different gradient-based and histogram-based edge detection algorithms using AVHRR SST data and made a comparison between SST fronts detected by algorithms and obtained from in situ data. They suggested that the SIED method performed better in providing accurate statistics of fronts occurrence at scales over 10 km, while the gradient method (based on the Sobel gradient operator) was better at scales below 10 km. So, for further frontal studies, gradient methods may be a better choice for detecting fine-scale fronts than the SIED method.

4.2. Trends of frontal activity (Aim 2)

The assessment of frontal activity of the two Australian hotspots (SE/SW) illustrate changes in recent years. Despite the influence of missing data (see Section 3.1), we can still draw reliable conclusions to confirm our hypothesis on trends. Firstly, the overall trends of frontal probability (PFEs) and frontal density (FD) all follow a gently-increasing monotonic trend. Although some of the increasing trends are not statistically significant based on the modified Mann-Kendall test, they have, to a certain extent, confirmed a gentle increase in frontal activity. According to the description of hotspots given by Hobday and Pecl (2014), the two hotspots are experiencing ocean warming. Therefore, there may be a positive correlation between increasing frontal activity and the warming ocean. In the SE study region, ocean warming appears to be related to the southward extension of the East Australia Current (EAC) (Ridgway 2007). Relying on series of measurements of SST and salinity, Willis et al. (2004) suggested that decadal-scale spin-up of the South Pacific Gyre, partly due to greenhouse warming and ozone depletion (Cai et al. 2005; Cai 2006), possibly contributed to the extension of EAC. Carrying tropical water, the southward and eastward flowing of EAC form strong eddies and fronts in the Tasman Sea, such as the Tasman Front (Godfrey et al. 1980; Andrews et al. 1980; Stanton 1981; Mulhearn 1987; Belkin & Cornillon 2003). The Tasman Front can also be the key to explain the spatial difference in PFE across latitudes in Figure 3.12 because it is where the EAC begins to meander east (~ 35°S), which may cause the difference in south-north stability of water masses (Belkin & Cornillon 2003). The southward extension of EAC means that more eddies and fronts will appear in the southern Tasman Sea (Oliver et al. 2015). This was also confirmed by an Ocean Eddy-resolving Model (OEM) used by Matear et al. (2013). Their model shows an increased EAC transport with increased eddy activity and the southward shift of the EAC. In the SW study region, frontal activity is largely impacted by two strong ocean currents, the West Australian Current (WAC) and the Leeuwin Current (LC). WAC is produced by the west wind drift on the southern Indian Ocean and transfers cold water from the Southern Ocean to the north. LC is inshore of WAC and transfers warm tropical water to the south. They flow in opposite directions and further cause strong convection in the SW study region. Their long-term changes in flow and location, as well as their correlation between each other, may all lead to increasing frontal activity. Taking LC as an example, LC has experienced a strengthening trend in the past two decades (Feng et al. 2009). However, it is likely due to natural decadal variability instead of long-term ocean warming because many climate models have suggested a weakened LC due to global warming (Feng et al. 2009). Both datasets we used for the SW study region did not cover enough years to observe long-term trends two decades ago. However, the increasing frontal activity of the SW study region does appear to be accompanied by ocean warming (Hobday & Pecl 2014) and the decadal-scale strengthening of LC (Feng et al. 2009).

Another important conclusion is the seasonal variability of frontal probability and density. This is fairly evident because the results of the two study regions show similar patterns. Both regions show high frontal activity in austral summer months and low frontal activity in winter months. This is shown in the plots of FD and monthly PFE in Figures 3.9, 3.11, 3.13 and 3.15. Seasonal variation of EAC and LC may contribute to the seasonal variation in frontal activity. In the SE study region, the EAC retracts north in winter (Frusher et al. 2014). As mentioned above, the overall southward extension of EAC brings more eddies and fronts to the South East Australia hotspot region. The retraction of EAC in winter will lead to the opposite result. For the SW study region, the seasonal cycle of frontal activity can be dominated by the seasonality of WAC and LC. Both of the currents have been confirmed to have significant seasonal cycles. WAC becomes weaker in winter and stronger in summer (Andrews 1979). LC also shows a seasonal cycle with maximum flow in May-June (Cresswell & Golding 1980; Feng et al. 2003). Due to the variation in the wind field, LC is weaker in summer and stronger in winter (Feng et al. 2003). The confluence of such seasonal currents may cause frontal activity to change seasonally. But for this region, there might be other potential causes, such as prevailing winds and seasonal precipitation, because it also covers part of the Indian Ocean beyond

WAC and LC.

Based on the results from high-quality MODIS, significant fluctuations appeared in the interannual trends of frontal activity may correlate to climate modes such as El Niño-Southern Oscillation (ENSO). The most significant fluctuation as mentioned is that the SE study region shows a low frontal activity in 2010 (see Figure 3.13c). This coincides with the 2010-2011 La Niña. We suspect this to be due to a smaller temperature difference between the tropical water transported by EAC and cold water in the Tasman Sea during a La Niña. On the one hand, during a La Niña, tropical water in the Pacific Ocean moves west (Philander 1985) and pours into the Tasman Sea, increasing the temperature of water masses. On the other hand, increasing cloud cover and rainfall over tropical regions reduce the temperature of water transported by EAC (Philander 1985). These then blur the SST boundary between EAC and cold water from the southern Tasman Sea and eventually frontal activity in the SE study region. However, this impact of ENSO needs to be studied further, because the AVHRR data results do not show significant changes in frontal activity during 2010.

Increasing trends in probability and density of fronts can have implications for marine biodiversity, fisheries and aquaculture. In the study of Matear et al. (2013), their OEM model simulated that an increasing eddy activity in the Tasman Sea, with the EAC's increasing transport and southward extension due to climate change, causes an increase in the nutrient supply to the upper ocean, as well as increases in phytoplankton concentrations and biological productivity. Due to the close relationship between frontal activity and eddy activity, an increase in frontal activity is likely to be accompanied by an increase in primary productivity and leading to increases in biomass (Rivas 2006). This will promote the redistribution of some commercially valuable species, such as southern bluefin tuna and yellowfin tuna (Hartog et al. 2011). Therefore, our results may be used for a variety of purposes, such as planning and managing fishery areas and quotas and aquaculture facilities site planning. Knowledge of patterns and trends in productivity related to frontal activity could be useful for determining suitable locations for offshore aquaculture facilities. The frontal maps produced in this study along with the trends can be used guide planning and management of these aquaculture sites and be used to assist in adaptive planning for climate change (Silva et al. 2012). As productivity shifts in both spatial patterns and temporal trends maps of frontal maps can also be useful to guide long-term fisheries strategies and policies to better integrate the impact of climate change on harvest levels (Chassot et al. 2011; Klemas 2013).

In addition to trends, frontal activity appears to have specific spatial distribution. Firstly, it is more frequent in coastal areas than offshore (see Figure 3.8, 3.10, 3.12 and 3.14). This is possibly due to more complex coastal conditions such as bathymetric features (Levine & White 1983; Wolanski & Hamner 1988; Wall et al. 2008) and the hydrodynamic influence of estuarine and riverine flux (Fischer et al. 2017). Secondly, Figures 3.12 and 3.14 show a significant latitudinal gradient in frontal probability; higher in the low latitudes and lower in the high latitudes. The variability of the strong currents mentioned above can be one of the causes of this gradient. For example, the eastward meandering of EAC near 35°S forms the Tasman Front which separates the warm water of the Coral Sea from the cold water of the Tasman Sea (Condie & Dunn 2006; Dambacher et al. 2012). Belkin and Cornillon (2003) suggested that the Tasman Front forms numerous meanders in the western and central Tasman Sea due to the EAC variability and topographic effects of ridges in the northern Tasman Sea (Andrews et al. 1980; Stanton 1981; Mulhearn 1987). According to Ridgway and Dunn (2003), the Tasman Front creates a complex marine environment with vertical mixing and eddies, which may correspond to high frontal probability in the low latitudes of the SE study region. The flow of the eastward meander is expected to increase with a flow reduction in the southward transport of EAC (Deng et al. 2011; Hill et al. 2011). For areas south of the Tasman Front (high-latitude area), due to the flow reduction of the southward EAC, water masses are relatively more stable than the low latitudes leading to low frontal probability. Assessing this impact requires further research because only the MODIS data results show the significant latitudinal gradient in frontal probability.

4.3. Future research

This study provides multiple directions for future research in frontal detection and trend analysis. Firstly, frontal detection methods need to be further evaluated with extensive data from ground-truthing surveys. Secondly, modelling efforts are needed to verify and demonstrate the correlation between increasing frontal activity and local potential biological activity and fisheries yields. For instance, the study of Rivas (2006) quantitatively estimated the correlation between thermal fronts and chlorophyll concentration. It was achieved by identifying small regions where the presence of a thermal front affects phytoplankton biomass and finding the relationship between surface chlorophyll concentration of these small regions and a larger region. This involves knowledge of marine processes and the response of phytoplankton to the effectiveness of light, temperature and nutrients. Therefore, the results of this study are expected to contribute to the building of predictive models for biodiversity based on thermal frontal activity. It will require clear satellite SST imagery corrected by in situ data, suitable and evaluated edge detection algorithm to produce clear thermal fronts and quantitative estimation of the response of biomass to changes in thermal fronts.

References

Andrews, JC 1979, *Eddy structure and the west and east Australian currents*, Research report of Flinders Institute for Atmospheric and Marine Sciences no. 30, Flinders University of South Australia, Adelaide.

Andrews, JC, Lawrence, MW & Nilsson, CS 1980, 'Observations of the Tasman Front', *Journal of Physical Oceanography*, vol. 10, no. 11, pp. 1854-1869, doi: 10.1175/1520-0485(1980)010<1854:OOTTF>2.0.CO;2.

Bakun, A 1990, 'Global climate change and intensification of coastal ocean upwelling', *Science*, vol. 247, no. 4939, pp. 198-201, doi: 10.1126/science.247.4939.198.

Belkin, IM 2002, 'Front', in JW Nybakken, WW Broenkow, TL Vallier (eds.), *Interdisciplinary Encyclopedia of Marine Sciences*, Grolier, Danbury, pp. 433–436.

Belkin, IM 2009, 'Observational studies of oceanic fronts', *Journal of Marine Systems*, vol. 78, pp. 317–318, doi: 10.1016/j.jmarsys.2008.10.016.

Belkin, IM, Cornillon, P & Sherman, K 2007, 'Fronts in Large Marine Ecosystems', *Progress in Oceanography*, vol. 81, no. 1-4, pp. 223-236, doi: 10.1016/j.pocean.2009.04.015.

Belkin, IM, & Cornillon, P 2003, 'SST fronts of the Pacific coastal and marginal seas', *Pacific Oceanography*, vol. 1, no. 2, pp. 90-113.

Belkin, IM, & Cornillon, P 2004, 'Surface thermal fronts of the Okhotsk Sea', *Pacific Oceanography*, vol. 2, no. 1-2, pp. 6–19.

Belkin, IM & O'Reilly, JE 2009, 'An algorithm for oceanic front detection in chlorophyll and SST satellite imagery', *Journal of Marine Systems*, vol. 78, pp. 319-326, doi: 10.1016/j.jmarsys.2008.11.018.

Bontempi, P & Yoder, J 2004, 'Spatial variability in SeaWiFS imagery of the South Atlantic bight as evidenced by gradients (fronts) in chlorophyll a and water-leaving radiance', *Deep Sea Research Part II: Topical Studies in Oceanography*, vol. 51, no. 10-11, pp. 1019-1032, doi: 10.1016/j.dsr2.2003.10.011.

Brandini, FP, Tura, PM & Santos, PGM 2018, 'Ecosystem responses to biogeochemical fronts in the South Brazil Bight', *Progress in Oceanography*, vol. 164, pp. 52-62, doi: 10.1016/j.pocean.2018.04.012.

Breaker, LC, Mavor, TP & Broenkow, WW 2005, *Mapping and monitoring large-scale ocean fronts off the california coast using imagery from the GOES-10 geostationary satellite*, University of California, San Diego.

Brink, KH 1987, 'Upwelling fronts: implications and unknowns', *South African Journal of Marine Science*, vol. 5, no. 1, pp. 3-9, doi: 10.2989/025776187784522315.

Cai, W 2006, 'Antarctic ozone depletion causes an intensification of the Southern Ocean super-gyre circulation', *Geophysical Research Letters*, vol. 33, no. L03712, doi:10.1029/2005GL024911.

Cai, W, Shi, G, Cowan, T, Bi, D & Ribbe, J 2005, 'The response of the Southern Annular Mode, the East Australian Current, and the southern mid-latitude ocean circulation to global warming', *Geophysical Research Letters,* vol. 32, no. L23706, doi:10.1029/2005GL024701.

Canny, J 1986, 'A computational approach to edge detection', *IEEE Transactions on Pattern Analysis and Machine Intelligence* ,vol. PAMI-8, no. 6, pp. 679-698, doi: 10.1109/TPAMI.1986.4767851.

Cayula, J, Cornillon, P, Holyer, R & Peckinpaugh, S 1991, 'Comparative study of two recent edge-detection algorithms designed to process sea-surface temperature fields', *IEEE Transactions on Geoscience and Remote Sensing*, vol. 29, no. 1, pp. 175-177, doi: 10.1109/36.103308.

Cayula, J & Cornillon, P 1992, 'Edge detection algorithm for SST images', *Journal of Atmosphere and Oceanic Technology*, vol. 9, no. 1, pp. 67-80, doi: 10.1175/1520-0426(1992)009<0067:EDAFSI>2.0.CO;2.

Cayula, J & Cornillon, P 1995, 'Multi-Image edge detection for SST images', Journal of Atmospheric and Oceanic Technology, vol. 12, no. 4, pp. 821-829, doi: 10.1175/1520-0426(1995)012<0821:MIEDFS>2.0.CO;2.

Chapman, CC, Lea, MA, Meyer, A, Sallée, JB & Hindell, M 2020, 'Defining Southern Ocean fronts and their influence on biological and physical processes in a changing climate', *Nature Climate Change*, vol. 10, pp. 209-219, doi: 10.1038/s41558-020-0705-4.

Chassot, E, Bonhommeau, S, Reygondeau, G, Nieto, K, Polovina, JJ, Huret, M, Dulvy, NK & Demarcq, H 2011, 'Satellite remote sensing for an ecosystem approach to fisheries management', *ICES Journal of Marine Science*, vol. 68, no. 4, pp. 651-666, doi: 10.1093/icesjms/fsq195.

Condie, SA 1993, 'Formation and stability of shelf break fronts', *Journal of Geophysical Research: Oceans*, vol. 98, no. C7, pp. 12405-12416, doi: 10.1029/93JC00624.

Condie, SA & Dunn, JR 2006, 'Seasonal characteristics of the surface mixed layer in the Australasian region: implications for primary production regimes and biogeography', *Marine and Freshwater Research*, vol. 57, no. 6, pp. 569-590, doi: 10.1071/MF06009.

Cresswell, GR & Golding, TJ 1980, 'Observations of a south-flowing current in the southeastern Indian Ocean', *Deep Sea Research Part A. Oceanographic Research Papers*, vol. 27, no. 6, pp. 449-466, doi: 10.1016/0198-0149(80)90055-2.

Dambacher, JM, Hosack, GR & Rochester, W 2012, *Ecological indicators for the exclusive economic zone of Australia's East Marine Region*, Report for the Australian Government Department of Sustainability, Environment, Water, Population and Communities, Commonwealth Scientific and Industrial Research Organisation, Canberra, doi: 10.4225/08/584c45092fc21.

Deng, X, Griffin, DA, Ridgway, KR, Church, JA, Featherstone, WE, White, NJ, Cahill, M 2011, 'Satellite Altimetry for Geodetic, Oceanographic, and Climate Studies in the Australian Region', in S Vignudelli, A Kostianoy, P Cipollini, J Benveniste (eds.), *Coastal Altimetry*, Springer-Verlag, Berlin, pp. 473-508, doi: 10.1007/978-3-642-12796-0_18.

Diehl, SF, Budd, JW, Ullman, DS & Cayula, J 2002, 'Geographic window sizes applied to remote sensing sea surface temperature front detection', *Journal of Atmospheric and Oceanic Technology*, vol. 19, no. 7, pp. 1105–1113, doi: 10.1175/1520-0426(2002)019<1105:GWSATR>2.0.CO;2.

Etnoyer, P, Canny D, Mate, BR, Morgan, LE, Ortega-Ortiz, JG & Nichols, WJ 2006, 'Sea-surface temperature gradients across blue whale and sea turtle foraging trajectories off the Baja California Peninsula, Mexico', *Deep Sea Research Part II: Topical Studies in Oceanography*, vol. 53, no. 3-4, pp. 340-358, doi: 10.1016/j.dsr2.2006.01.010.

Feng, M, Meyers, G, Pearce, A & Wijffels, S 2003, 'Annual and interannual variations of the Leeuwin Current at 32°S', *Journal of Geophysical Research: Oceans*, vol. 108, no. C11, doi: 10.1029/2002JC001763.

Feng, M, Weller, E & Hill, K 2009, 'The Leeuwin Current', in ES Poloczanska, AJ Hobday, AJ Richardson (eds.), *Marine Climate Change Impacts and Adaptation Report Card for Australia 2009*, National Climate Change Adaptation Research Facility, Gold Coast.

Fiedler, PC & Bernard, HJ 1987, 'Tuna aggregation and feeding near fronts observed in satellite imagery', *Continental shelf research*, vol. 7, no. 8, pp. 871-881, doi: 10.1016/0278-4343(87)90003-3.

Fischer, AM, Ryan, JP & Rienecker, EV 2017, 'Fine scale mapping of the structure and composition of the Elkhorn Slough (California, USA) tidal plume' , *Estuarine, Coastal and Shelf Science*, vol. 184, pp. 10–20, doi: 10.1016/j.ecss.2016.10.035.

Frusher, SD, Hobday, AJ, Jennings, SM, Creighton, C, D'Silva, D, Haward, M, Holbrook, NJ, Nursey-Bray, M, Pecl, GT & Putten, EI 2014, 'The short history of research in a marine climate change hotspot: from anecdote to adaptation in south-east Australia', *Reviews in Fish Biology and Fisheries*, vol. 24, pp. 593–611, doi: 10.1007/s11160-013-9325-7.

Godfrey, JS, Cresswell, GR, Golding, TJ & Pearce, AF 1980, 'The separation of the East Australian current', *Journal of Geophysical Research: Oceans*, vol. 121, no. 1, pp. 758-774, doi: 10.1002/2015JC011133.

Hartog, J, Hobday, A, Matear, R & Feng, M 2011, 'Habitat overlap between southern bluefin tuna and yellowfin tuna in the east coast longline fishery––Implications for present and future spatial management', *Deep Sea Research Part II: Topical Studies in Oceanography*, vol. 58, no. 5, pp. 746-752, doi: 10.1016/j.dsr2.2010.06.005.

Heath, RA 1972, 'Wind-derived water motion off the east coast of New Zealand', *New Zealand Journal of Marine and Freshwater Research*, vol. 6, no. 3, pp. 352-364, doi: 10.1080/00288330.1972.9515430.

Hickox, R, Belkin, IM, Cornillon, P & Shan, Z 2000, 'Climatology and seasonal variability of ocean fronts in the East China, Yellow and Bohai seas from satellite SST data', *Geophysical Research Letters*, vol. 27, no. 18, pp. 2945-2948, doi: 10.1029/1999GL011223.

Hill, K, Rintoul, SR, Ridgway, KR & Oke, PR 2011, 'Decadal changes in the South Pacific western boundary current system revealed in observations and reanalysis state estimates', *Journal of Geophysical Research: Oceans*, vol. 116, no. C01009, doi: 10.1029/2009JC005926.

Hobday, AJ & Pecl, GT 2014, 'Identification of global marine hotspots: sentinels for change and vanguards for adaptation action' , *Reviews in Fish Biology and Fisheries*, vol. 24, pp. 415–425, doi: 10.1007/s11160-013-9326-6.

Holladay, CG & O'Brien, JJ 1975, 'Mesoscale variability of sea surface temperature' , *Journal of Physical Oceanography*, vol. 5, no. 4, pp. 761-772, doi: 10.1175/1520-0485(1975)005<0761:MVOSST>2.0.CO;2.

Holyer, RJ & Peckinpaugh, SH 1989, 'Edge detection applied to satellite imagery of the oceans', *IEEE Transactions on Geoscience and Remote Sensing*, vol. 27, no. 1, pp. 46-56, doi: 10.1109/36.20274.

Huo, YK, Wei, G, Zhang, YD & Wu, LN 2010, 'An adaptive threshold for the Canny Operator of edge detection', *2010 International Conference on Image Analysis and Signal Processing*, Institute of Electrical and Electronics Engineers, New Jersey, US, pp, 371-374, doi: 10.1109/IASP.2010.5476095.

Integrated Marine Observing System (IMOS) 2019, *IMOS - SRS - SST - L3S - Single Sensor - 6 day - day time - Australia*, Australian Bureau of Meteorology, Melbourne, Dataset, viewed 29 November 2019, <https://portal.aodn.org.au/search>.

Joseph, A 2014, 'Oceanic currents and their implications', in A Joseph (ed.), *Measuring Ocean Currents*, Elsevier, Amsterdam, pp. 1-49, doi: 10.1016/B978-0-12-415990-7.00001-6.

Joseph, A 2017, 'Magic with colors—sea surface changes', in A Joseph (ed.), *Investigating Seafloors and Oceans*, Elsevier, Amsterdam, pp. 555-574, doi: 10.1016/B978-0-12-809357-3.00010-2.

Kahru, M, Di Lorenzo, E, Manzano-Sarabia, M & Mitchell, BG 2012, 'Spatial and temporal statistics of sea surface temperature and chlorophyll fronts in the California Current', *Journal of Plankton Research*, vol. 34, no. 9, pp. 749– 760, doi:10.1093/plankt/fbs010.

Kahru, M, Jacox, MG & Ohman, MD 2018, 'CCE1: Decrease in the frequency of oceanic fronts and surface chlorophyll concentration in the California Current System during the 2014–2016 northeast Pacific warm anomalies', *Deep Sea Research Part I: Oceanographic Research Papers*, vol. 140, pp. 4–13, doi: 10.1016/j.dsr.2018.04.007.

Kim, YS & Orsi, AH 2014, 'On the variability of Antarctic Circumpolar Current fronts inferred from 1992-2011 altimetry', *Journal of Physical Oceanography*, vol. 44, no. 12, pp. 3054-3071, doi: 10.1175/JPO-D-13-0217.1.

Klemas, V 2013, 'Fisheries applications of remote sensing: an overview', *Fisheries Research*, vol. 148, pp. 124-136, doi: 10.1016/j.fishres.2012.02.027.

Landry, MR, Ohman, MD, Goericke, R, Stukel, MR, Barbeau, K, Dundy, R & Kahru, M 2012, 'Pelagic community responses to a deep-water front in the California Current Ecosystem: overview of the A-Front Study', *Journal of Plankton Research*, vol. 34, no. 9, pp. 739–748, doi: 10.1093/plankt/fbs025.

Lekouara, M 2013, 'Exploring frontogenesis processes in new satellite sea surface temperature data sets', PhD thesis, University of Southampton, Southampton.

Letelier, J, Pizarro, O & Nunez, S 2009, 'Seasonal variability of coastal upwelling and the upwelling front off central Chile', *Journal of Geophysical Research: Oceans*, vol. 114, no. C12009, doi: 10.1029/2008JC005171.

Levine, ER & White, WB 1983, 'Bathymetric influences upon the character of North Pacific Fronts, 1976–1980', *Journal of Geophysical Research: Oceans*, vol. 88, no. C14, pp. 9617-9625, doi: 10.1029/JC088iC14p09617.

Matear, RJ, Chamberlain, MA, Sun, C & Feng, M 2013, ‘Climate change projection of the Tasman Sea from an Eddy-resolving Ocean Model’, *Journal of Geophysical Research: Oceans*, vol. 118, no. 6, pp. 2961– 2976, doi:10.1002/jgrc.20202.

Mauzole, YL, Torres, HS & Fu, LL 2020, ‘Patterns and Dynamics of SST Fronts in the California Current System’, *Journal of Geophysical Research: Oceans*, vol. 125, no. 2, doi: 10.1029/2019JC015499.

Miltiadou, M, Papoutsa, C, Karathanassi, V, Kolokoussis, P, Lafon, V, Sykas, D, Sarelli, A, Prodromou, M & Hadjimitsis, D 2018, ‘Detection of marine fronts: a comparison between different approaches applied on the SST product derived from Sentinel-3 data’, *Sixth International Conference on Remote Sensing and Geoinformation of the Environment (RSCy2018)*, Society of Photo-Optical Instrumentation Engineers, Washington, US, no. 1077305, doi: 10.1117/12.2324126.

Mulhearn, PJ 1987, ‘The Tasman Front: A study using infrared imagery’, *Journal of Physical Oceanography*, vol. 17, no, 8, pp. 1148-1155, doi: 10.1175/1520-0485(1987)017<1148:TTFASU>2.0.CO;2.

Obenour, KM 2013, ‘Temporal trends in global sea surface temperature fronts’, Master thesis, University of Rhiode Island, Rhode Island.

Ocean Biology Processing Group (OBPG) 2015, *MODIS Aqua Level 3 SST Thermal IR 8 Day 4km Daytime v2014.0*, Physical Oceanography Distributed Active Archive Center (PO.DAAC), California, Dataset, viewed 27 February 2020, <https://doi.org/10.5067/MODSA-8D4D4>.

Oerder, V, Bento, J, Morales, C, Hormazabal, S & Pizarro, O 2018, ‘Coastal Upwelling Front Detection off Central Chile (36.5–37°S) and Spatio-Temporal Variability of Frontal Characteristics’, *Remote Sensing*, vol. 10, no. 5, doi: 10.3390/rs10050690.

Oliver, ECJ, Donat, MG, Burrows, MT, Moore, PJ, Smale, DA, Alexander, LV, Benthuysen, JA, Feng, M, Gupta, AS, Hobday, AJ, Holbrook, NJ, Perkins-Kirkpatrick, SE, Scannell, HA, Straub, SC & Wernberg, T 2018, ‘Longer and more frequent marine heatwaves over the past century’, *Nature Communications*, vol. 9, no. 1324, doi: 10.1038/s41467-018-03732-9.

Oliver, ECJ, O'Kane, TJ & Holbrook, NJ 2015, 'Projected changes to Tasman Sea eddies in a future climate', *Journal of Geophysical Research: Oceans*, vol. 120, no. 11, pp. 7150–7165, doi: 10.1002/2015JC010993.

Orfanidis, SJ 1996, *Introduction to Signal Processing*, Prentice-Hall, Englewood Cliffs.

Otsu, N 1979, 'A threshold selection method from gray-level histograms', *IEEE Transactions on Systems, Man, and Cybernetics*, vol. 9, no. 1, pp. 62-66, doi: 10.1109/TSMC.1979.4310076.

Patakamuri, SK & O'Brien, N 2019, 'Modified Versions of Mann Kendall and Spearman's Rho Trend Tests', Version 1.4.1, R package, <https://CRAN.R-project.org/package=modifiedmk>.

Pereira, FL, Sousa, JB, Martins, CG & da Silva, EP 1995, 'AUV system requirements for coastal oceanography', *'Challenges of Our Changing Global Environment' OCEANS '95 MTS/IEEE,* Institute of Electrical and Electronics Engineers, New Jersey, US, vol. 3, pp. 1651-1658, doi: 10.1109/OCEANS.1995.528732.

Philander, SGH 1985, 'El Niño and La Niña', *Journal of the Atmospheric Sciences*, vol. 42, no. 23, pp. 2652-2662, doi: 10.1175/1520-0469(1985)042<2652:ENALN>2.0.CO;2.

Prewitt, J 1970, 'Object enhance and extraction', *Picture Processing and Psychopictorics*, pp. 75-149.

Ridgway, KR 2007, 'Long-term trend and decadal variability of the southward penetration of the East Australian Current', *Geophysical Research Letters*, vol. 34, no. 13, doi:10.1029/2007GL030393.

Ridgway, KR & Dunn, JR 2003, 'Mesoscale structure of the mean East Australian Current System and its relationship with topography', *Progress in Oceanography*, vol. 52, no. 2, pp. 189-222, doi: 10.1016/S0079-6611(03)00004-1.

Rivas, AL 2006, 'Quantitative estimation of the influence of surface thermal fronts over chlorophyll concentration at the Patagonian shelf', *Journal of Marine Systems*, vol. 63, no. 3-4, pp. 183-190, doi: 10.1016/j.jmarsys.2006.07.002.

Robbins, IC, Kirkpatrick, GJ, Blackwell, SM, Hillier, J, Knight, CA & Moline, MA 2006, 'Improved monitoring of HABs using autonomous underwater vehicles (AUV)', *Harmful Algae*, vol. 5, no. 6, pp. 749-761, doi: 10.1016/j.hal.2006.03.005.

Roberts, JJ, Best, Bd, Dunn, DC, Treml, EA & Halpin, PN 2010, 'Marine Geospatial Ecology Tools: An integrated framework for ecological geoprocessing with ArcGIS, Python, R, MATLAB, and C++', *Environmental Modelling and Software*, vol. 25, no. 10, pp. 1197-1207, doi: 10.1016/j.envsoft.2010.03.029.

Robinson, LS 2010, *Discovering the Ocean from Space: The unique applications of satellite*, Springer/Praxis Publishing, Berlin.

Roden, GI 1976, 'On the structure and prediction of oceanic fronts', *Naval Research Reviews*, vol. 29, pp. 18-35.

Royer, F, Fromentin, J & Gaspar, P 2004, 'Association between bluefin tuna schools and oceanic features in the western Mediterranean', *Marine Ecology Progress Series,* vol. 269, pp. 249–263, doi: 10.3354/meps269249.

Sallée, JB, Speer, K & Morrow, R 2008, 'Response of the Antarctic Circumpolar Current to atmospheric variability', *Journal of Climate*, vol. 21, no. 12, pp. 3020-3039, doi: 10.1175/2007JCLI1702.1.

Saraceno, M, Provost, C & Piola, AR 2005, 'On the relationship between satelliteretrieved surface temperature fronts and chlorophyll a in the western South Atlantic', *Journal of Geophysical Research*, vol. 110, no. C11016, doi:10.1029/2004JC002736.

Sato, M, Barth, JA, Benoit-Bird, KJ, Pierce, SD, Cowles, TJ, Brodeur, RD & Peterson, WT 2018, 'Coastal upwelling fronts as a boundary for planktivorous fish distributions', *Marine Ecology Progress Series*, vol. 595, pp.171-186, doi: 10.3354/meps12553.

Shrivakshan, GT & Chandrasekar, C 2012, 'A Comparison of various Edge Detection Techniques used in Image Processing', *International Journal of Computer Science Issues*, vol. 9, pp. 269-276.

Silva, C, Barbieri, MA, Yáñez, E, Gutiérrez-Estrada, JC & DelValls, TÁ 2012, 'Using indicators and models for an ecosystem approach to fisheries and aquaculture management: the anchovy fishery and Pacific oyster culture in Chile: case studies', *Latin American Journal of Aquatic Research*, vol. 40, no. 4, pp. 955-969, doi: 10.3856/vol40-issue4-fulltext-12.

Snyder, S, Franks, PJ, Talley, LD, Xu, Y & Kohin, S 2017, 'Crossing the line: Tunas actively exploit submesoscale fronts to enhance foraging success', *Limnology and Oceanography Letters*, vol. 2, no. 5, pp. 187-194, doi: 10.1002/lol2.10049.

Sobel, I & Feldman, G 1973, 'An isotropic 3x3 image gradient operator', *Pattern Classification and Scene Analysis*, pp. 271-272.

Stanton, BR 1981, 'An oceanographic survey of the Tasman Front', *New Zealand Journal of Marine and Freshwater Research*, vol 15, no. 3, pp. 289-297, doi: 10.1080/00288330.1981.9515924.

Stegmann, PM & Ullman, DS 2004, 'Variability in chlorophyll and sea surface temperature fronts in the Long Island Sound outflow region from satellite observations', *Journal of Geophysical Research: Oceans*, vol. 109, no. C07S03, doi: 10.1029/2003JC001984.

Stukel, MR, Aluwihare, LI, Barbeau, KA, Chekalyuk, AM, Goericke, R, Miller, AJ, Ohman, MD, Ruacho, A, Song, H, Stephens, BM & Landry, MR 2017, 'Mesoscale ocean fronts enhance carbon export due to gravitational sinking and subduction' , *Proceedings of the National Academy of Sciences,* vol. 114, no. 6, pp. 1252–1257, doi: 10.1073/pnas.1609435114.

Ullman, DS & Cornillon, P 1999, 'Satellite-derived sea surface temperature fronts on the continental shelf off the northeast U.S. coast', *Journal of Geophysical Research: Oceans*, vol. 104, no. C10, pp. 23459– 23478, doi:10.1029/1999JC900133.

Ullman, DS & Cornillon, P 2000, 'Evaluation of Front Detection Methods for Satellite-Derived SST Data Using In Situ Observations', *Journal of Atmospheric and Oceanic Technology*, vol. 17, no. 12, pp. 1667-1675, doi: 10.1175/1520-0426(2000)017<1667:EOFDMF>2.0.CO;2.

Ullman, DS & Cornillon, P 2001, 'Continental shelf surface thermal fronts in winter off the northeast US coast', *Continental Shelf Research*, vol. 21, no. 11-12, pp. 1139-1156, doi: 10.1016/S0278-4343(00)00107-2.

Vázquez, DP, Atae-Allah, C & Escamilla, PL 1999, ‘Entropic approach to edge detection for SST images’, *Journal of Atmospheric and Oceanic Technology*, vol. 16, no. 7, pp. 970–979, doi: 10.1175/1520-0426(1999)016<0970:EATEDF>2.0.CO;2.

Wai, MMK & Stage, SA 1989, ‘Dynamical analyses of marine atmospheric boundary layer structure near the Gulf Stream oceanic front’, *Quarterly Journal of the Royal Meteorological Society*, vol. 115, no. 485, pp. 29-44, doi: 10.1002/qj.49711548503.

Wall, CC, Muller-Karger, FE, Roffer, MA, Hu, C, Yao, W & Luther, ME 2008, ‘Satellite remote sensing of surface oceanic fronts in coastal waters off west-central Florida’, *Remote Sensing of Environment*, vol. 112, no. 6, pp. 2963-2976, doi: 10.1016/j.rse.2008.02.007.

Williams, RG, Wilson, C & Hughes, CW 2007, ‘Ocean and atmosphere storm tracks: the role of eddy vorticity forcing’, *Journal of Physical Oceanography*, vol. 37, no. 9, pp. 2267–2289, doi: 10.1175/JPO3120.1.

Willis, JK, Roemmich D & Cornuelle, B 2004, ‘Interannual variability in upper ocean heat content, temperature, and thermosteric expansion on global scales’, *Journal of Geophysical Research: Oceans*, vol. 109, no. C12036, doi:10.1029/2003JC002260.

Wolanski, E & Hamner, WM 1988, ‘Topographically controlled fronts in the ocean and their biological influence’ , *Science*, vol. 241, no. 4862, pp. 177–181, doi: 10.1126/science.241.4862.177.

Woodson, CB & Litvin, SY 2015, ‘Ocean fronts drive marine fishery production and biogeochemical cycling’, *Proceedings of the National Academy of Sciences*, vol. 112, no. 6, pp. 1710–1715, doi: 10.1073/pnas.1417143112.

Xu, Y, Nieto, K, Teo, SL, McClatchie, S & Holmes, J 2017, ‘Influence of fronts on the spatial distribution of albacore tuna (Thunnus alalunga) in the Northeast Pacific over the past 30 years (1982–2011)’, *Progress in Oceanography*, vol. 150, pp. 72-78, doi: 10.1016/j.pocean.2015.04.013.

Yue, S & Wang, CY 2004, ‘The Mann-Kendall test modified by effective sample size to detect trend in serially correlated hydrological series’, *Water Resources Management*, vol. 18, no. 3, pp. 201-218, doi: 10.1023/B:WARM.0000043140.61082.60.

Zhang, Y, Ryan, JP, Godin, MA & Bellingham, JG 2012, 'Observing coastal upwelling front dynamics by AUV tracking, remote sensing, and mooring measurements', *2012 American Geophysical Union Fall Meeting Abstracts*, pp. OS31H-04.